NTNU – Trondheim
Norwegian University of
Science and Technology

Correlation of Catalyst Morphology with Attrition Resistance and Catalytic Activity of Fischer-Tropsch Catalysts

Thomas Haukli Fiske

Chemical Engineering and Biotechnology
Submission date: June 2013
Supervisor: Magnus Rønning, IKP
Co-supervisor: Erling Rytter, Statoil
Sigrid Eri, Statoil

Norwegian University of Science and Technology
Department of Chemical Engineering

1 Declaration

I declare that this is an independent work according to the exam regulations at the Norwegian University of Science and Technology (NTNU).

Thomas Haukli Fiske

2 Preface

A hectic, but very interesting period of working with this specialization project and master thesis is nearing the end. It has been an educational and rewarding year, which eventually has led to this report you now are holding.

All the work associated with this report was conducted throughout the spring semester of 2013. The experimental work described was performed at the Statoil Research Centre at Rotvoll, and at NTNU Gløshaugen. This project was iniated by my supervisors Professor Magnus Rønning from NTNU, and Erling Rytter and Sigrid Eri from Statoil.

I would like to thank Statoil ASA for providing excellent laboratories with instruments and raw materials needed for the experiments. A special thanks to all the helpful and inspiring people working at Rotvoll. Sigrid Eri and Torild Hulsund Skagseth; I am really grateful for all the assistance regarding training on the instruments and other experimental work in the laboratory. The theoretical discussions on an almost daily basis has also been of major help, so thank you both. Erling Rytter and Edvard Bergene; You have been of great help with theoretical insight and advice during our monthly meetings. This has given me an enhanced understanding of the theoretical principles, which has proven to be essential for interpreting the experimental results. I will also like to thank Rune Myrstad at Sintef for performing the activity testing of the catalyst, and Øyvind Borg for training on the chemisorption apparatus.

A special thank you is dedicated to my supervisors Professor Magnus Rønning and Adjunct Professor Erling Rytter for giving this master thesis proposal. It has been a great experience, and I hope to get to use my knowledge developed through this work in the future.

3 Abstract

Three alumina based support materials for the Fischer-Tropsch synthesis (FTS) catalyst has been prepared and investigated. The three support materials were prepared in order to obtain different mechanical strengths, henceforth denoted weak, medium and strong support. Magnesium modified $\gamma - alumina$ support material calcined at 950° C and 1050° C were prepared as the medium and strong support respectively, whereas the unmodified alumina was used as the weak support. The modified support materials were both prepared by the incipient wetness impregnation method to obtain 10 wt.% Mg. Several batches were prepared to gain enough material for the planned experiments.

Each of the support materials were subject to one crushing process in order to try to alter the particle morphology. The chosen method was determined based on the results from the specialization project. In this project, one method gave a larger change in morphology than other methods. Therefore a ball mill was the method of choice. Unprocessed samples and samples subjected to the ball mill for the three different materials were tested for attrition in an attrition rig, and characterized in terms of morphology using a particle analyzer. The different fractions were also analyzed with respect to particle morphology using an environmental scanning electron microscope (ESEM). FTS catalysts with 12 wt.% Co and 0,5 wt.% Re were prepared from the weak and the medium support materials, both unprocessed and milled fractions, using the incipient wetness impregnation. These four catalyst samples were tested for dispersion using a chemisorption experiment, and for activity and selectivity using a dedicated setup.

Results from the particle analyzer showed that the morphology had not been altered as much as expected. Most change in shape occurred for the medium strength support material, but the observed alteration was much less than observed for the same experiment in the specialization project. For the weaker

and stronger support, only a slight change was observed, and for the strong support material this change was in the direction of rounder particles. This is probably due to the excellent mechanical strength of the strong support, which leads to grinding of the kinks and corners of the particles and not the breakage of whole particles to smaller and more uneven fragments. With such relative small differences in morphology between the unprocessed and the milled materials, correlations of morphology with other parameters are difficult to obtain. The same correlation as from the specialization project, with rounder particles having a higher attrition resistance, was observed. A slight degree of correlation was also found between particle morphology and dispersion, where more uneven particles gave a slightly higher value of cobalt dispersion.

4 Sammendrag

Tre aluminabaserte bærere for Fischer-Tropsch syntese (FTS) ble fremstilt og undersøkt. De tre bærermaterialene ble fremstilt for å oppnå forskjellige mekaniske styrker, heretter betegnet svak, middels og sterk bærer. Magnesium-modifisert $\gamma - alumina$ bærermateriale kalsinert ved 950° C og 1050° C ble fremstilt henholdsvis som middels og sterk bærer, mens ikke-modifisert alumina ble anvendt som den svake bæreren. De modifiserte bærermaterialene ble begge fremstilt ved *incipient wetness* impregneringsmetoden for å oppnå 10 vekt.% Mg. Flere partier ble preparert for å få nok materiale til de planlagte eksperimentene.

De tre bærermaterialene ble utsatt for en knuseprosess for å forsøke og endre partikkelmorfologien. Den valgte metoden ble bestemt basert på spesialiseringprosjektet, og hvilke av disse metodene som endret morfologien mest. Derfor ble en kulemølle valgt som metode. Ubehandlede fraksjoner, og fraksjonene utsatt for knusing i mølle for de tre forskjellige materialene, ble testet for slitasjemotstand i en dedikert rigg, og karakterisert med hensyn til morfologi ved hjelp av en partikkelanalysator. De forskjellige fraksjonene ble også analysert med hensyn til partikkelmorfologi ved hjelp av et elektronmikroskop (ESEM). FTS-katalysatorer med 12 vekt.% Co og 0,5 vekt.% Re ble fremstilt fra det svake og det middels sterke bærermaterialet, både ubehandlet og knust fraksjon, med incipient wetness-impregnering. Disse fire katalysatorprøvene ble testet for dispersjon ved hjelp av et kjemisorpsjonseksperiment, og for aktivitet og selektivitet ved hjelp av et dedikert oppsett.

Resultater fra partikkelanalysatoren viste at morfologien ikke var endret så mye som forventet. Mesteparten av endringen i form ble observert for bæreren med middels styrke, men den observerte forandringen var mindre enn det som ble observert for det samme eksperimentet i fordypningsprosjektet. For svak og sterk bærer ble bare en liten endring observert, og for det sterke bærermaterialet var denne endringen i retning av rundere partikler. Dette er

trolig på grunn av den imponerende mekaniske styrken til den sterke bæreren, noe som fører til nedsliping av hjørner og uregelmessigheter på partiklene, og ikke at den brytes ned til mindre og mer ujevne fragmenter. Med slike relativt små forskjeller i morfologi mellom det ubehandlede og det knuste materialet, er korrelasjoner av morfologi med andre parametre vanskelig å oppnå. Den samme korrelasjonen som fra spesialiseringsprosjektet, hvor rundere partikler har en høyere slitasjemotstand, ble observert. En liten grad av korrelasjon ble også funnet mellom partikkelmorfologi og dispersjon, hvor mer ujevne partikler ga en litt høyere verdi av kobolt-dispersjon.

List of Figures

List of Tables

Contents

5 Introduction

5.1 Natural gas and the search for cleaner fuel

Natural gas is an important energy resource in the world today. The energy demand is increasing worldwide, and the global society is continuously looking for new and more environmentally friendly energy sources. Increase in global energy demand towards 2030, with respect to energy source is reported as shown in Figure 5.1.

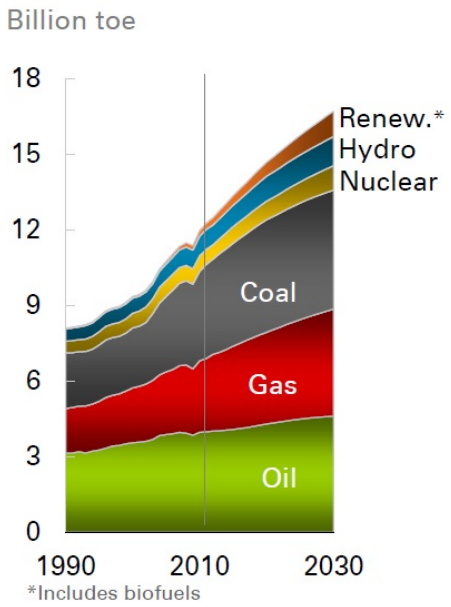

Figure 5.1: Predicted global energy consumption by source [1]

With the population growth and increasing standard of living, the largest leap in energy consumption is assigned to power production. In addition, the energy consumption in the transport sector will also increase as shown in Figure 5.2.

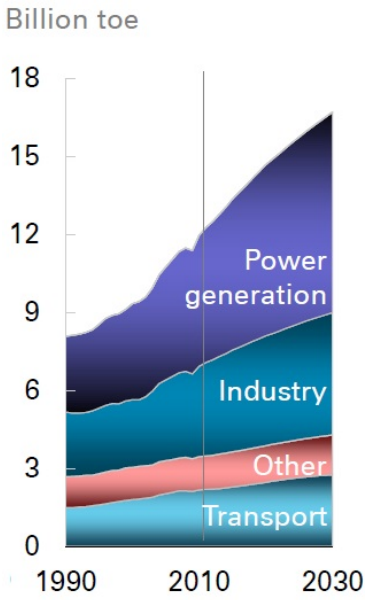

Figure 5.2: Predicted global energy consumption by primary use [1]

One of the main challenges in the years to come is to meet the needs in the transport sector. This is due to an increase in fuel usage, and the fact that the oil reserves are limited. It is therefore need to look for alternatives in producing fuels to the transport sector. One option is to use natural gas. Natural gas can be converted to liquid fuels through a technology known as gas-to-liquids (GTL). In this technology, natural gas is reformed to synthetic gas by steam reforming or autothermal reforming (ATR) followed by a synthesis step known as the Fischer-Tropsch synthesis (FTS). The FTS yields a wax consisting of long-chained alkanes and alkenes, which has to be further treated (hydrocracking etc) and separated to produce diesel or other fuels. A simple schematic of the GTL process is depicted in Figure 5.3.

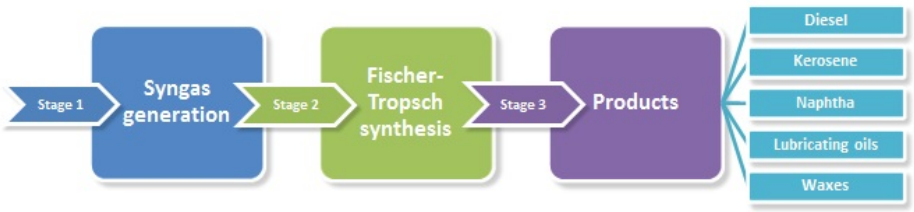

Figure 5.3: Simple schematic of GTL process [2]

The Fischer-Tropsch process was developed by the German scientists Franz Fischer and Hans Tropsch in 1923, and was extensively used by the Germans to produce fuel during World War II [15]. Both alkanes and alkenes are produced in the process, shown respectively by:

$$\mathrm{xCO} + (2x+1)\mathrm{H_2} \longrightarrow \mathrm{C_xH_{2x+2}} + \mathrm{xH_2O}$$

$$\mathrm{xCO} + 2\,\mathrm{xH_2} \longrightarrow \mathrm{C_xH_{2x}} + \mathrm{xH_2O}$$

A sketch of the different reaction pathways of the FT process is illustrated in Figure 5.4.

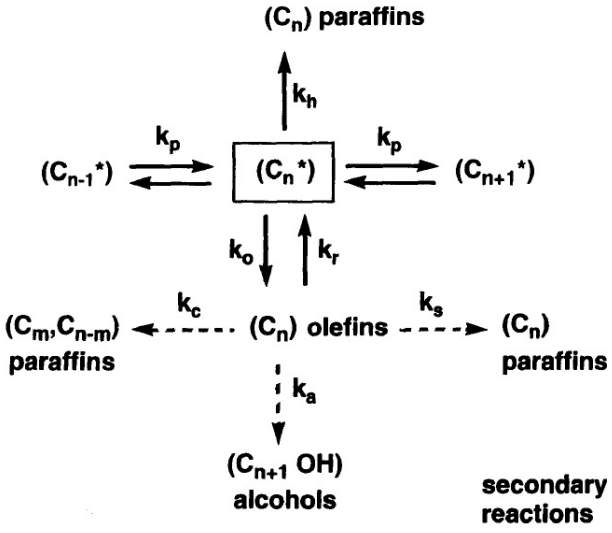

Figure 5.4: Sketch of the FT process [3]

A renewed interest for FT-based fuels has emerged due to the possibility to produce cleaner fuel from natural gas, and thereby also utilize natural gas at remote oilfields where no pipelines for gas is present [15]. This would present an option to flaring of the natural gas, which is hazardous to the environment. Fuels produced from the FT synthesis are practically sulfur-free, which lowers the emissions of SO_2 and SO_3. In addition it does not contain aromatics. Aromatics in traditional diesel fuel promote unwanted particulate formation that is emitted to the local environment. This renewed interest has also reached the media. The Norwegian technical magazine Teknisk Ukeblad published an informative article on the subject last year [16].

The financial aspect is always important in the industry, and the future of the GTL technology is dependent on its economical viability. An important

factor in this is the price of the feedstock, thus the price of crude oil and natural gas. These prices vary from day to day, and are influenced by many different factors. The viability of commercial FT plants have been heavily dependent on the crude oil price, and a historical chart of the crude oil price from 1970 to 2000 is shown in Figure 5.5.

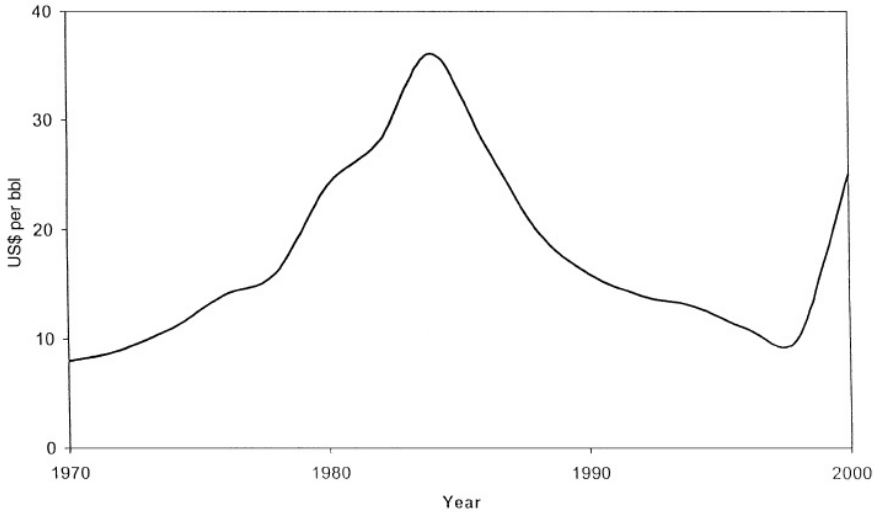

Figure 5.5: Crude oil price [4]

The oil crisis in the 1970‘s led to a steep increase in the crude oil price, which resulted in two coal-based FT plants in South Africa. Since the turn of the millennium, the price of crude oil has just steadily increased and is now about 100 dollars per barrel. With such high crude oil prices, the GTL technology and the including FT process look more and more promising.

5.2 Catalysts for the Fischer-Tropsch synthesis

A good catalyst for the FT synthesis, like for most other industrial processes, has to meet several criteria:

- High activity
- Good selectivity towards long chained alkanes/alkenes (C_{5+})
- Sufficient lifetime

When it comes to the first requirement, only the metals Fe, Ni, Co and Ru have satisfactory results for commercial purposes [4]. Nickel-based catalysts produce too much CH_4 under operating conditions, and thereby fails the second criteria. When also considering economical aspects, ruthenium is way too expensive, and therefore leaves iron and cobalt as the preferred active metals for the FT process. To increase reducibility of the catalyst, rhenium is often added as a promoter. Which of the two metals to use as catalyst depends on the raw material. If the raw material is coal, Fe is the recommended choice as it exhibits good activity for the water gas shift (WGS) reaction.

$$CO + H_2O \rightleftharpoons CO_2 + H_2$$

Coal-based synthesis gas has a low H_2/CO ratio, and therefore needs a high WGS activity [17]. A feed of natural gas on the other hand results in a desirable H_2/CO ratio. No WGS activity is needed for the FT process with natural gas as the feedstock, and Co is therefore the recommended catalyst.

The third demand for a good FT catalyst is the lifetime. The lifetime of a catalyst is mainly dependent on two factors:

- Deactivation mechanisms for the active metal
- Mechanical strength of the support

There are many deactivation mechanisms involved in this process. Poisoning, re-oxidation of active sites, carbidization and sintering are some of them [18]. Mechanical strength of the support is important in terms of attrition resistance. In fluidized bed reactors and slurry bubble columns, which are the preferred reactor systems for FT synthesis, attrition is highly relevant. The particles are undergoing a lot of physical stress that eventually leads to particle breakdown. Al_2O_3 (alumina) is a widely used support because of its good mechanical properties and stability. One way to further increase the attrition resistance is to impregnate the support with another metal before calcination [6]. Adding for instance magnesium results in a material with improved crushing strength (attrition resistance). This is due to the formation of a magnesium aluminate, $MgAl_2O_4$, spinel structure upon heat treatment (high temperature calcination). This will prevent the formation of the inactive cobalt aluminate, which is formed during high temperature calcination. In the spinel structure of $MgAl_2O_4$ oxygen ions are packed in a FCC structure, with Mg in tetrahedral sites and Al in octahedral sites [15]. The pure Al_2O_3 is cation deficient which leads to defects. The lack of these defects gives the $MgAl_2O_4$ better attrition resistance.

5.3 Scope of this thesis

The scope of this thesis is to investigate if it can be found a correlation between the morphology of catalyst support particles and the attrition of these particles, and if there exists a correlation between morphology of the Fischer-Tropsch (FT) catalyst and the catalytic activity. Investigation of the activity, selectivity and lifetime of the FT catalyst is of great importance for the commercialization of the GTL technology. To be able to compete financially with fuels produced from oil, FT catalysts need to be improved in order to make the process more economical and energy efficient. Designing a catalyst support material with high attrition resistance will yield a catalyst with increased lifetime and a less polluted wax product. Only a small increase in the activity and/or the selectivity of the catalyst could have a huge impact on the viability compared to the oil-based fuels, so such correlations studied here are therefore possibly very interesting. In order to investigate these correlations, three different alumina supports with different material strengths will be tested. Unmodified, commercial alumina will be used as the weak support, and magnesium modified alumina calcined at 950° C and 1050° C will be used as the medium and strong support respectively.

6 Theory

In this section, relevant theory regarding particle attrition and particle analysis is given. Also, theory on experimental techniques such as BET surface area and chemisorption measurements are presented. An understanding of the underlying theoretical principles is essential for interpreting and discussing the obtained results.

6.1 Particle attrition

Particle attrition is a commonly occurring problem in the chemical process industry, and especially in the field of catalysis. Attrition is defined as the unwanted breakdown of particles [19], and is often caused by collisions between particles and the walls of reactors or vessels. This unwanted breakdown can be divided into two terms, abrasion and fragmentation. Removal of small parts of the original particle like corners or surface layers is defined as abrasion, whereas splitting into a large number of smaller particles is defined as fragmentation. The causes of particle attrition have been debated. Earlier it was believed that attrition mainly was due to hydrodynamic forces, whereas other stresses like chemical stress and thermal stress was neglected [20]. Today it is believed that catalyst particles and catalyst pellets can undergo attrition through various stresses, as shown in Figure 6.1.

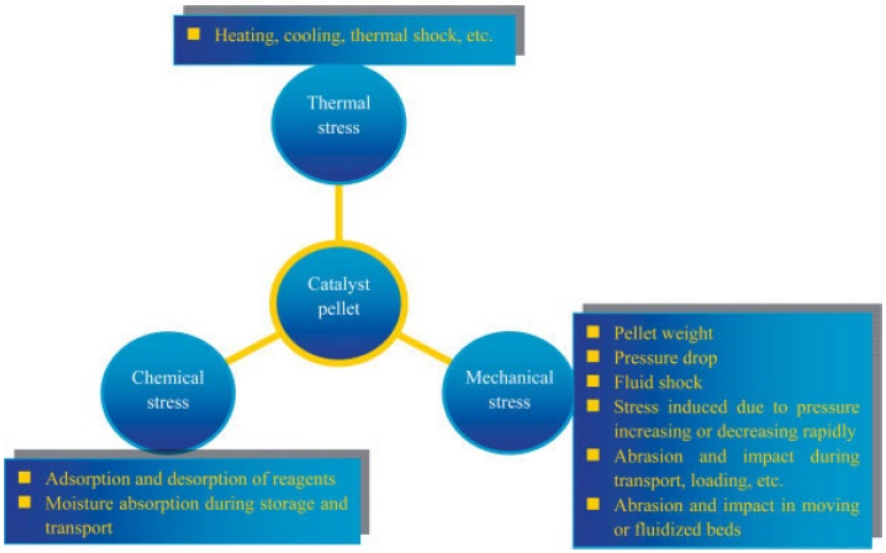

Figure 6.1: Various stresses which causes attrition [5]

Attrition of catalyst particles is a problem in the industry for two reasons:

- The lifetime of the catalyst is lowered
- The products are contaminated by fines

These are major industrial concerns. In the Fischer-Tropsch synthesis, the produced wax can be severely contaminated by fines, as depicted in Figure 6.2.

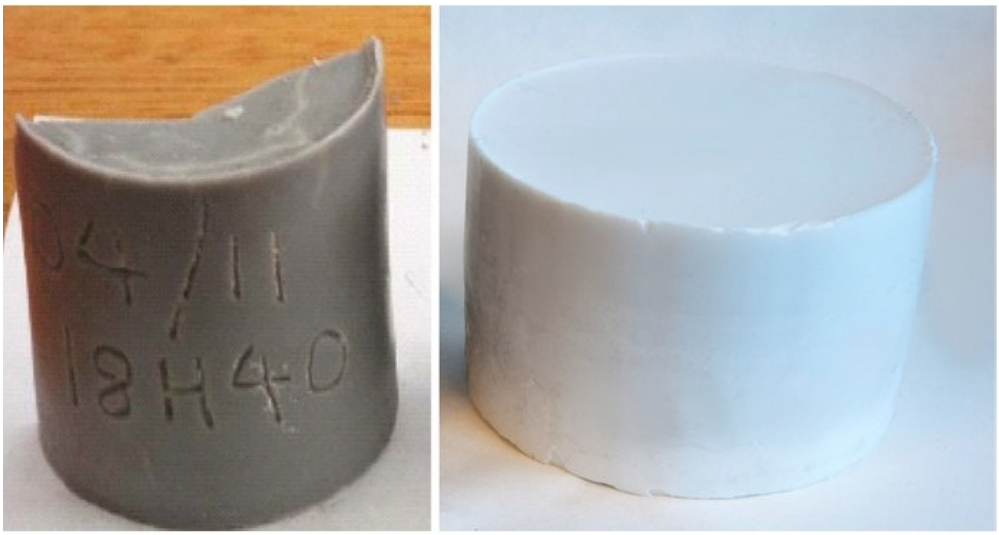

Figure 6.2: Product contaminated by fines (left) [6]

Both particle properties and properties connected to the industrial chemical process effect the degree of attrition. The shape of a particle can influence attrition. Generally it is understood that irregular particles suffer more from abrasion, as they consist of more corners and kinks than spherical particles. Fragmentation is more independent of particle shape. When it comes to particle size, the answer becomes more complicated. Larger particles are easier to break down than smaller particles, but the relationship between attrition and particle size depends on the process and the material.

When it comes to other parameters in which attrition is affected, time and pressure are highly relevant. Most often a linear relationship between time and attrition is not observed. The rate of attrition is higher in the beginning of the attrition process, and this is due to an early fragmentation of the weaker particles. After fragmentation of the weak particles, a linear relationship between time and abrasion is settled. The effect of pressure upon attrition is a more complex matter. In some systems, the attrition rate will increase with increasing pressure as this leads to more collisions between the

particles. On the other hand, attrition through abrasion may increase with decreasing pressure. Decreasing pressure lowers the density of the air around the particles, resulting in a higher velocity. Therefore the pressure should be kept at a constant level when comparing attrition rates of different materials.

To measure the extent of attrition a fluidized bed system is often used. The attrition rate as a function of time can be measured using an apparatus equipped with a high velocity humidified air stream. The air stream causes the particles to collide with each other and the walls of the apparatus, and the produced fines can be collected and weighed. Many of these systems look similar to the one developed by Gwyn [7] , and a sketch is shown in Figure 6.3.

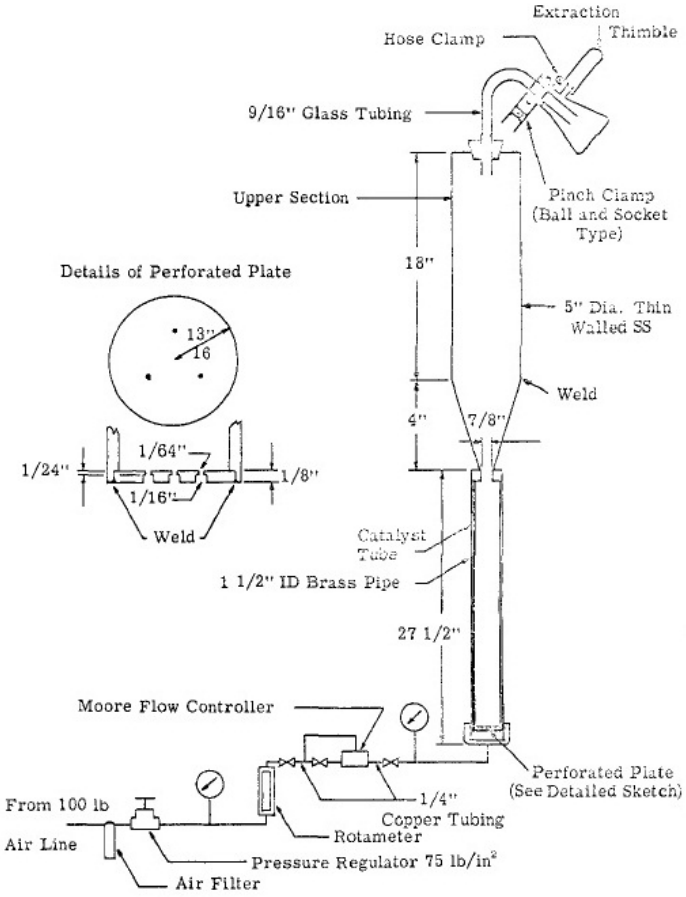

Figure 6.3: Attrition apparatus [7]

6.2 Particle analysis

The particle size distribution (PSD) and the morphology of particles can be measured by a particle analyzing instrument. One such instrument is the Camsizer XT by Retsch Technology [21]. The Camsizer XT is a particle characterization apparatus which takes use of digital image processing. Dynamic digital image analysis uses particles moving relative to a camera, and can analyze a large number of particles in a brief period of time. The stream of particles moves through a light source, whose shadows are detected by the camera. The Camsizer XT uses a two-camera system, with a basic camera taking pictures of large amounts of bigger particles and a zoom camera capturing smaller particles with a high resolution. This gives a wide measuring range going from 1 μm up to 3 nm. An illustration of this measurement system is given in Figure 6.4.

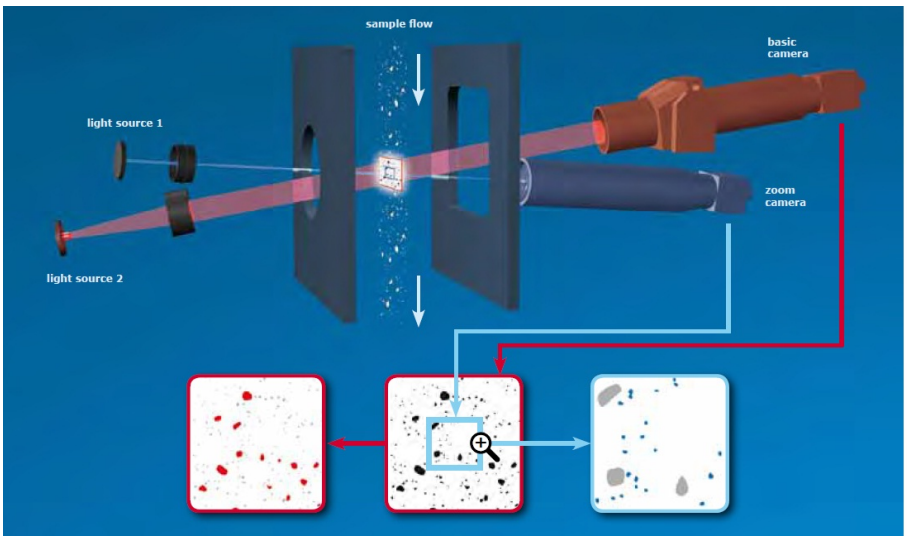

Figure 6.4: Camsizer XT Measurement system [8]

Particle size distribution can be measured on the basis of three different particle size definitions:

- $X_{c,min}$: The shortest maximum chord of the particle projection measured from all directions
- X_{area}: The diameter of a circle with the same projected area as the measured particle size
- $X_{Fe,max}$: The maximum distance between two tangents perpendicular to the measuring direction (Feret-diameter)

In addition to measure the particle size distribution, the Camsizer XT also measures different parameters related to particle shape. The parameter used in this study will be:

- Width/length ratio:

$$b/l = \frac{X_{c,min}}{X_{Fe,max}} \tag{6.1}$$

This parameter is often called the aspect ratio, and provides information about the lengthening of a particle. A b/l value of 1 represents a spherical particle. A sketch of a particle with b/l ratio < 1 is given in Figure 6.5.

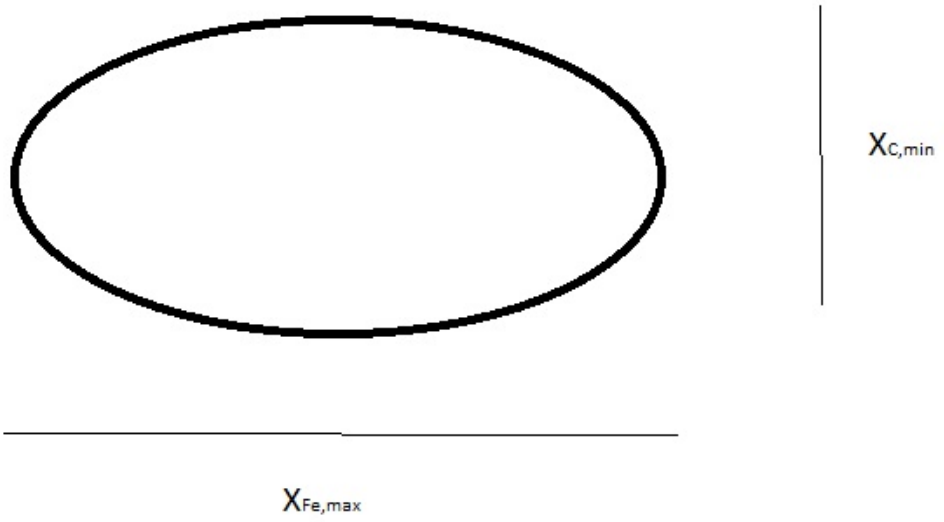

Figure 6.5: Particle with b/l ratio < 1

6.3 Surface area and pore structure

The surface area of a catalyst (often given as m^2/g) is one of the most important textural parameters for a catalyst support. It is often connected to the dispersion of active metal on the support, and thereby important for the catalytic activity. Measurements of the surface area takes advantage of the phenomena of physical adsorption, where weak Van Der Waals forces are responsible for the adsorption [22]. Nitrogen molecules are often used as probe molecules for these measurements. The adsorbed molecules will first form a monolayer, which at low pressures follow the Langmuir isotherm equation [22]:

$$\frac{V}{V_M} = \frac{K * p/p_0}{(1 + K * p/p_0)} \tag{6.2}$$

where V_m is the monolayer volume, p_0 is the saturation pressure of the adsorbed species and the K is the ratio between the rate constants for adsorption and desorption respectively.
Physical adsorption has the ability to go beyond monolayer and form multilayers. This was theorized by Brunauer, Emmett and Teller in the famous BET equation [23]:

$$\frac{V}{V_M} = \frac{C * p}{[p_0 - p] * [1 + (C - 1) * p/p_0]} \tag{6.3}$$

where the parameter C involves the heats of adsorption.

An alumina support usually has a specific surface area of about $50 - 300 m^2/g$ [15] depending on which phase it occurs in, which is dependent on temperature. This is illustrated in Figure 6.6.

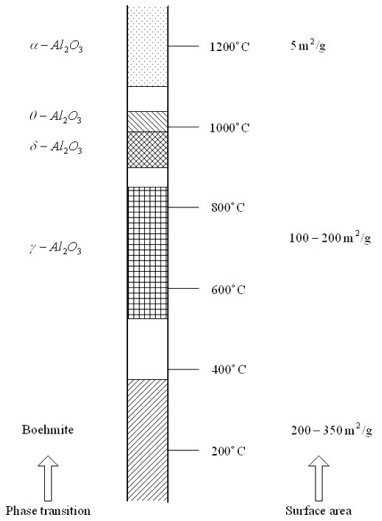

Figure 6.6: Alumina phase change and surface area [9]

Pores in the support material can be divided into [15]:

- **Micropores**: pore width less than 2 nm
- **Mesopores**: pore width 2-50 nm
- **Macropores**: pore width more than 50 nm

During the adsorption of nitrogen, condensation in the mesopores can occur. The pore radius, r, can then be calculated by the Kelvin Equation [22]:

$$r = \frac{2SVcos\theta}{RTln(p_0/p)} \tag{6.4}$$

where S is the surface tension of liquid N_2, V is the molar volume, θ is the contact angle, R is the gas constant and T is the temperature.

6.4 Environmental Scanning Electron Microscopy

Environmental Scanning Electron Microscope (ESEM) is a version of the more known Scanning Electron Microscope (SEM), and the governing principles behind these two instruments are similar. It consists of an electron column which creates a beam of electrons, sample chamber, detectors and image constructing system [10]. An electron gun accelerates the electrons towards the sample with high energies (thousands of eV). The beam is then deflected in a scanning pattern and focused on the sample surface. The sample is penetrated by the beam and emits energy. Different emitted signals are detected and used to create an image. The interaction between the beam and the sample is shown in Figure 6.7.

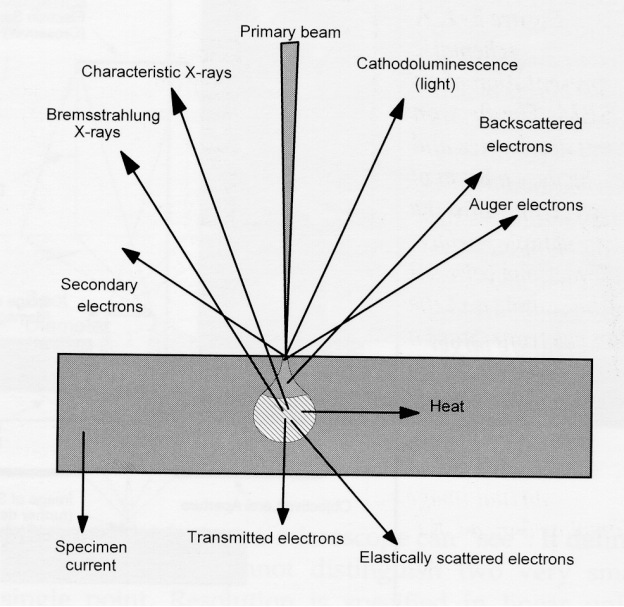

Figure 6.7: Beam interacting with sample [10]

The main difference between the ESEM and the conventional SEM is that the ESEM uses multiple pressure limiting apertures (PLA), while the SEM

only uses a single PLA to separate the sample chamber from the column. The ESEM also uses a different detector, an Environmental Secondary Detector (ESD), that can function in a non-vacuum environment. Benefits of the ESEM are no need for sample preparation, and the fact that it can handle wet, oily and dirty samples [10]. The drawback is a lower image resolution than the SEM, but for particles of some size the resolution is acceptable.

6.5 Chemisorption and measurement of dispersion

Chemisorption is an adsorption process that is very different from the physical adsorption described in Section 6.3. Whereas physical adsorption is due to weak Van der Waals forces, chemisorption is the existence of strong valence bonds between the adsorbed gas and the solid surface [24]. Chemisorption accordingly has a higher heat of adsorption, and are adsorbed at specific points at the surface in a monolayer. There are two types of chemisorption, dissociative and associative. Dissociative adsorption is when the adsorbing molecule has to dissociate, like is the case with adsorption of hydrogen gas. Associative adsorption is the case when the whole molecule adsorbs to the surface.

Selective chemisorption is a technique that can be used to determine the total number of surface atoms which are available for adsorption. This measurement is used to calculate the dispersion of the active metal on the catalyst. Dispersion is defined as [24]:

$$D = \frac{N_s}{N_t} \tag{6.5}$$

where N_s is the number of metal surface atoms and N_t is the total number of metal atoms in the sample.

Hydrogen gas is frequently used for selective chemisorption, due to its dissociative adsorption qualities. One hydrogen molecule bonds to two surface metal atoms, which is an easy stoichiometry. With an adsorption stoichiometry of F, the dispersion is given as [24]:

$$D = \frac{V_m * M * F}{x} \tag{6.6}$$

where V_m is the amount of adsorbed gas on the monolayer, M is the molar mass of the metal and x is the weight fraction of metal. It is assumed that hydrogen adsorbs dissociatively on cobalt, and that the hydrogen does not adsorb on the rhenium. To obtain the amount of adsorbed gas, a technique called volumteric chemisorption of hydrogen is often used. In this experiment, a small sample of the catalyst is exposed to adsorption of hydrogen gas at different pressures. As a result of this, an adsorption isotherm of physiosorption + chemisorption is obtained. The sample is then evacuated to remove the reversible adsorbed gas. Then, the procedure is repeated with similar conditions. The new adsorption isotherm will contain only the reversible adsorbed gas, and thus the amount of irreversible chemisorbed gas will be the difference between these two isotherms. These prinicples are depicted in Figure 6.8.

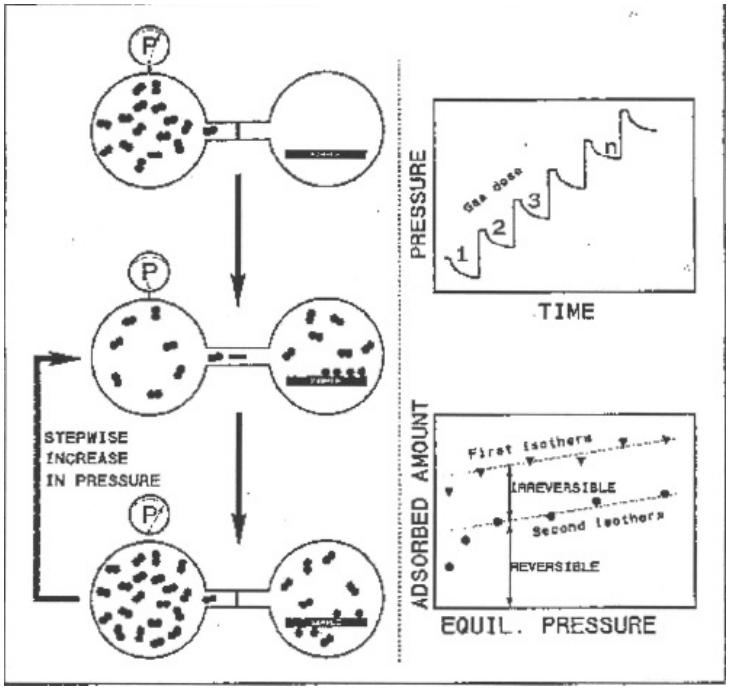

Figure 6.8: Volumetric chemisorption [11]

With information about the chemisorbed amount of gas, the dispersion can be calculated from Equation 6.6. The dispersion can be used to calculate the cobalt particle size. By using the data for the surface area of the cobalt from the chemisporption together with assuming a certain site density, we obtain this relation between cobalt particle size and dispersion [25]:

$$d = \frac{96,2}{D} \tag{6.7}$$

where d is the cobalt particle diameter in nanometers, and D is the dispersion given in percent.

7 Experimental

This chapter explains how the three different alumina supports were prepared, characterized and tested. It provides information about how the morphology was altered by a chosen method of crushing, and how the the attrition testing was performed. Information regarding the impregnation of the catalysts is also given here. Most of the experimental work described in this chapter was conducted at Statoil R&D centre at Rotvoll, Trondheim. The only exception is the activity testing of the catalysts, which was performed in a designated setup at NTNU, Gløshaugen. ESEM imaging was performed by Torild Hulsund Skagseth at Rotvoll.

7.1 Preparation of support

Both of the magnesium modified alumina supports were prepared by a one-step incipient wetness impregnation method. Steps for this method used in this study are described below.

1. 100 g of commercial γ-alumina was weighed in an evaporating dish
2. The amount of $Mg(NO_3)_2 \cdot 6\,H_2O$ to obtain 10 wt.% Mg was calculated. Calculations are shown in Appendix A.2.
3. The magnesium nitrate was dissolved in calculated amount of distilled water. Calculations are shown in Appendix A.1.
4. The solution was added in the dish containing the support. Mixed carefully with a glass spatula and knocked dish to reappear water.
5. Section 4 was repeated three times.
6. Dried at 110° C for 3 h. Stirred every 15 min the first hour, then every 30 min.
7. Medium strength support calcined at 950° C for 10 h, strong support calcined at 1050° C for 10 h

This preparation procedure was performed two times for the strong support in order to obtain enough material for the characterization and impregnation of the catalyst. For the medium strength support, material prepared for the specialization project was used. The method for altering the morphology of the three alumina supports was chosen in light of the results from the specialization project in the fall, and thus the ball mill became the method of choice. A picture of a laboratory ball mill is shown in Figure 7.1.

Figure 7.1: Laboratory Ball Mill [12]

The sample was put in a container together with methyl acrylate balls, and the container was fastened in the mill. 50 g of sample were milled at a time, and each fraction was milled for 90 min. Five methyl acrylate balls were used, and a picture of such balls is shown in Figure 7.2.

Figure 7.2: Methyl acrylate balls [13]

The point of milling is to grind larger particles down to smaller fractions. This is a frequently used operation in the process industry to obtain smaller particles [26]. The sample particles collide with the walls and the grinding balls, and are thereby broken down to smaller fractures by impact energy (fragmentation).

7.2 Nitrogen adsorption/desorption isotherm

To obtain information related to the surface characteristics of the three alumina supports, the N_2 adsorption/desorption isotherm of the basis (before crushing) was performed. Liquid N_2 at the boiling point ($-196°$ C [27]) in a Micrometrics TriStar 3000 instrument was used for the experiment. A sample of about 0,5 g was weighed in a sample tube and set to drying under vacuum at 250° C for 2-3 hours. The two samples were cooled before starting the instrument. Liquid nitrogen was filled in the tank, the samples were attached to the instrument and the experiment started. After the isotherm had been measured, the samples were weighed again and the software used the weights to calculate the BET surface area from Equation (6.3) and the pore size paramters from Equation (6.4).

7.3 Attrition test

The testing of attrition resistance of the six fractions (basis + milled fraction of each support) was performed in a rig which is a Statoil built modification of the apparatus in Figure 6.3. This rig consists of the following parts:

- Air supplying system
- Reactor tube
- Separation chamber
- Soxhlet filter

The rig operates in the following way: Air passes through a pressure regulator (5 bar) to a wetting unit to obtain around 30 % relative humidity. This

is to prevent static electricity in the system. The air flow is adjusted in a mass flow controller (MFC) to about 10 L/min before it is led to the reactor tube. Passage to the reactor tube is through a hole plate with three holes of diamter 0,4 mm. The input pressure at about 2,7 bar gives the pressurized air a velocity in the range of the sound velocity. Particles will collide with each other and the walls, and the small fines will go up to the separation chamber and be collected in the Soxhlet filter. It is important to sieve out particles smaller than 38 μm to prevent clogging of the holes in the hole plate. This could affect the pressure and the velocity of the air stream. The procedure itself was performed in the following order:

1. Sample was sieved for 60 min
2. 50 g of sample was weighed in a glass beaker
3. The empty collection tube was weighed and attached to the vessel
4. The separation tube was attached to the air inlet
5. 50 g of sample was added to the tube
6. The separation tube was attached to the vessel
7. The pressurized air flow and shaker was turned on
8. Air flow and shaker turned off and collection tube weighed every hour

7.4 Camsizer XT

For measurements of the particle size distribution and the morphology of the particles, the Camsizer XT from Retsch Technologies was used. A description of the theoretical aspects of the measurments is given in Chapter 6.2. The Camsizer XT consists of three dispersion modules. For fine powders, the X-Jet module is recommended. A sketch of the module is given in Figure 7.3.

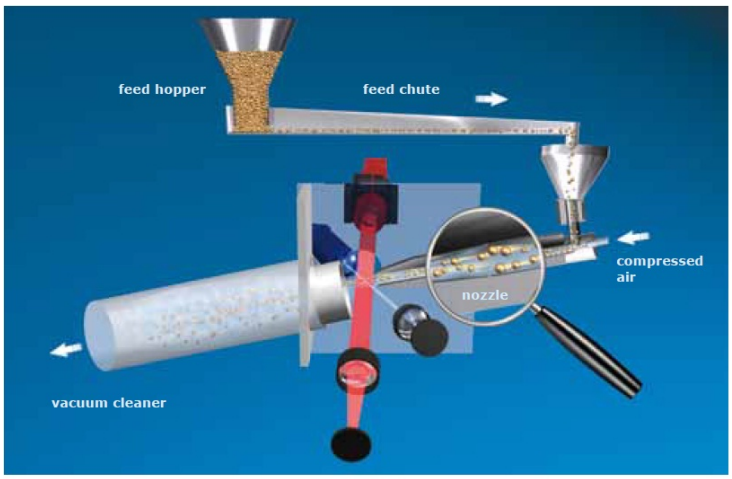

Figure 7.3: X-Jet module [8]

The sample is fed to the funnel, and is carried along the feed chute (which is vibrating) to a funnel where compressed air accelerates the particles through a nozzle. The amount of sample has to be large enough to obtain a representative distribution. A small amount of sample (2-4 g) is sufficient. Before the instrument is started, a task file in the included software has to be created. This is easily done, and most parameters are pre-programmed. The pressure of the compressed air can be altered, and its purpose is to prevent agglomeration of the particles. Agglomeration of such small particles is due

to the effects of Van der Waals forces or electrostatic charges. The minimum pressure of 20 kPa was sufficient to prevent agglomeration for this material. After the particles have been analyzed by the two-camera system, they end up in a vacuum cleaner. The associated software was used to collect size and shape characteristics in tables and graphs.

7.5 ESEM

Environment scanning electron microscopy (ESEM) was performed on the five fractions to give a good visual image of the morphology of the particles. An ordinary SEM could be used as well, but ESEM was chosen due to availability. Small amounts of sample were loaded on the sample stage and inserted into the instrument. Images of different resolutions were studied in order to assist the interpretation of the results from the Camsizer XT and the attrition rig. The ESEM was iniated to see whether or not cracks in the particles could be observed. A sketch of the ESEM is shown in Figure 7.4.

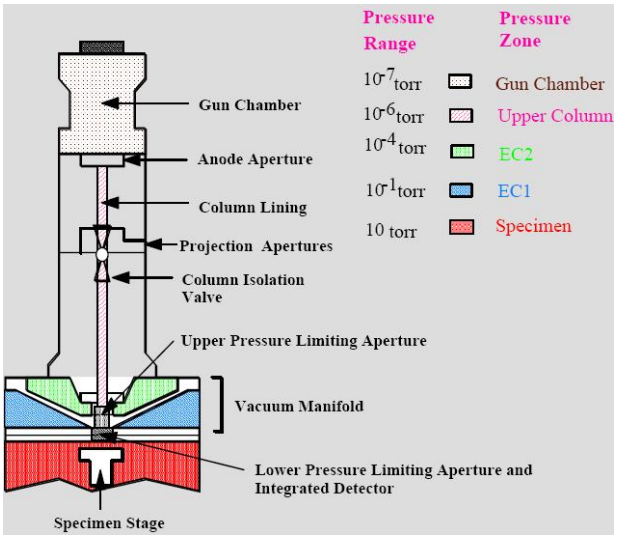

Figure 7.4: Environmental scanning electron microscope [14]

7.6 Impregnation of catalyst

To investigate if there exists a correlation between the catalyst activity and morphology of the catalyst support for the Fischer-Tropsch catalyst, the chosen supports were impregnated with cobalt and rhenium. Since the activity testing of the FT catalysts was limited to four samples, the unprocessed and milled fractions of the weak and medium support were chosen. The preparation of the catalysts was carried out using a one step incipient wetness impregnation. Water absorptivity for the magnesium aluminate was found by dropwise adding water to the point where all the pores were filled. This could be observed by overlayer water when knocking the evaporating dish. The calculations for water absorptivity are shown in Appendix A.1. The individual steps are shown below.

1. Approximately 20 g of support was weighed in an evaporating dish
2. The amount of cobalt salt ($Co(NO_3)_2 \cdot 6\,H_2O$) to obtain 12 wt.% Co was calculated. Calculations are shown in Appendix A.3.
3. The amount of rhenium acid ($HReO_4$) to obtain 0,5 wt.% Re was calculated. Calculations are shown in Appendix A.3.
4. The cobalt salt was dissolved in calculated amount of rhenium acid and distilled water.
5. The solution was added in the dish containing the support. Mixed carefully with a glass spatula and knocked dish to reappear water.
6. Section 5 was repeated three times.
7. Dried at 110° C for 3 h. Stirred every 15 min the first hour, then every 30 min.
8. Calcined at 300° C for 16 h.

7.7 Chemisorption

In order to measure the metal dispersion of the prepared catalysts, chemisorption with hydrogen was performed. This was done using a Micrometrics ASAP 2020 apparatus, which is depicted in Figure 7.5.

Figure 7.5: Chemisorption apparatus [11]

Before the analysis, the catalyst sample was sieved to obtain the fraction between 53 μm and 90 μm. The steps of the chemisorption procedure are shown below.

1. Ca 0,5 g of sample was weighed in and loaded, together with quartz wool to keep it in place, to a U-shaped tube reactor.
2. The sample was dried in vacuum at 225° C for two hours.
3. Transferred the setup to the analysis part of the apparatus
4. A leak test was performed by evacuating the sample, and then measuring the pressure increase when turning off vacuum.

5. Inserted sample information (weight, cobalt loading) in the software.
6. Started the analysis program and let it run until adsorption isotherm was obtained
7. Weighed the sample and inserted the new weight into the software
8. Collected the report from the software

7.8 Activity testing in FT setup

The testing of catalytic activity and selectivity of the prepared catalysts was performed by Rune Myrstad, research scientist Sintef. This was performed in a dedicated setup at NTNU, Gløshaugen. The procedure is thoroughly described in [28]. Because of limited capacity, only three of the four prepared catalysts were tested. It was chosen to test if there could be a diffrence in activity and/or selectivity between the alumina based support (weak) and magnesium aluminate based support (medium), and between the milled and unprocessed fraction of the medium support.

8 Results and discussion

The results and accompanying interpretations of the conducted experiments are given in this chapter. The associated calculations and numerical data are given in appendices.

8.1 BET results

The results of the measurements described in Chapter 7.2 are listed in Table 8.1

Table 8.1: BET results

Support	**BET**(m^2/g)	**Pore volume**(cm^3/g)	**Pore diameter**(Å)
Weak	162	0,69	115
Medium	94	0,46	141
Strong	49	0,24	135

Surface areas of these magnitudes are typical for alumina supports ($50 - 300m^2/g$ [15]), and the other two parameters correspond nicely as well. The surface area is related to the calcination temperature, with decreasing surface areas as the calcination temperature is increased. This is due to the phase transistions of alumina. Increasing the temperature gives a larger fraction of crystalline α-alumina with low surface areas. With a calcination temperature of 950° C, most should be in the γ-form and some may be in the θ-form or δ-form. For the strong support with a calcination temperature of 1050° C, most of it should be in the θ-form, but some of it may be in the α-form.

8.2 Attrition test

In this sub chapter, the results from the attrition tests of the three supports are presented. The value used for comparing attrition is easily calculated, and the calculations are shown in A.4. Values of attrition are shown in Table 8.2.

Table 8.2: Attrition values

Sample	**Fines (g)**	**Sample weight (g)**	**Attrition (%)**
Weak basis	3,52	50,84	6,92
Weak milled	7,01	50,20	13,96
Medium basis	2,54	50,09	5,07
Medium milled	4,28	50,04	8,55
Strong basis	0,80	50,11	1,60
Strong milled	0,64	50,16	1,28

As can be seen from the table, the attrition values of the three different basis materials are in accordance with the assumed material strengths of the supports. Another observation that can be made from this table is that for the weak and medium support, the attrition values increase for the milled fraction, whereas for the strong support it decreases. The results for the medium support (Mg aluminate calcined at 950° C) are comparable with the results from the specialization project in the fall, indicating good reproducibility of this analysis method.

Measurements of the amount of fines were done every hour for the whole 5 hour run. The mass of produced fines as a function of time for the three supports, basis and milled, is plotted as depicted in Figure 8.1 and Figure 8.2, respectively.

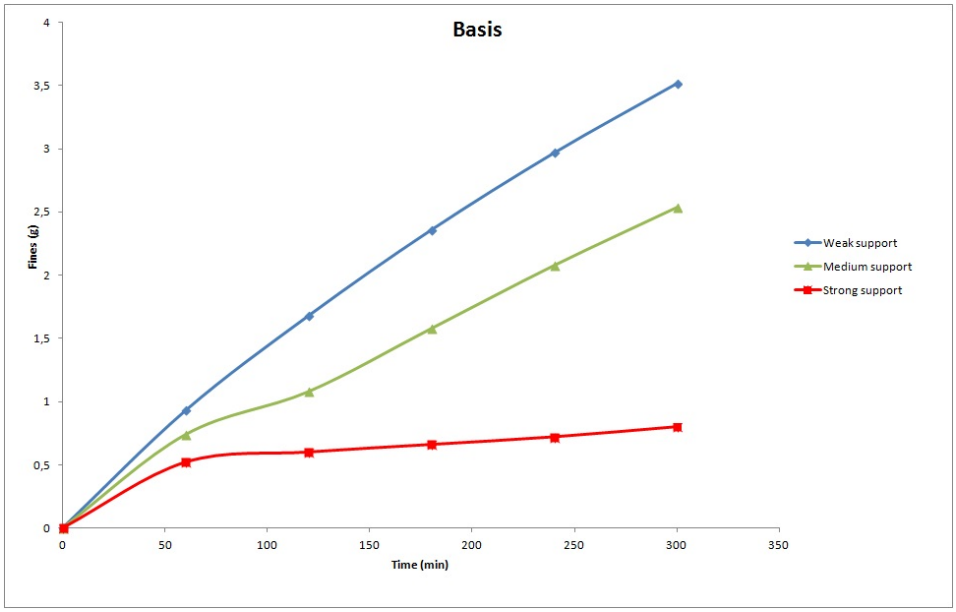

Figure 8.1: Attrition over time, basis

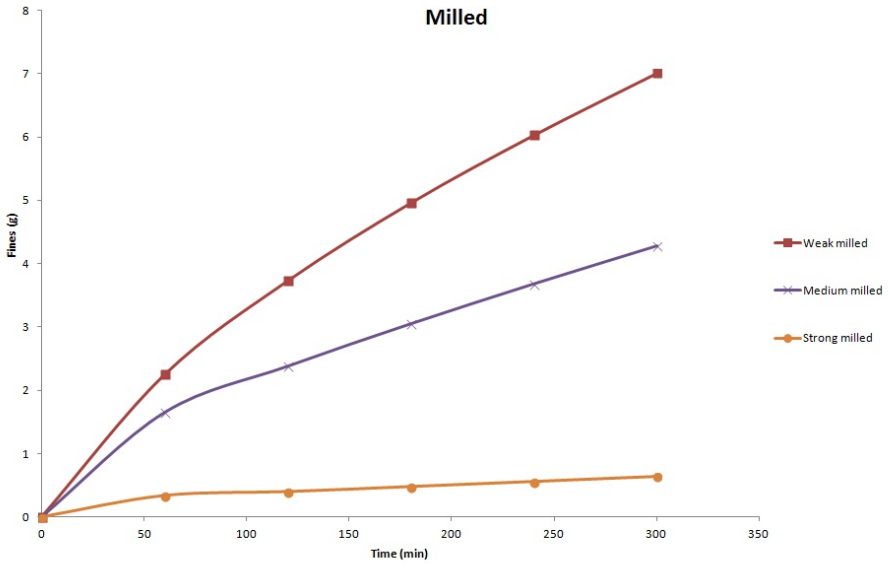

Figure 8.2: Attrition over time, milled

These graphs present some interesting information about the underlying attrition mechanisms. All lines are non-linear, with a steeper curve the first two hours before it flattens out for the last three. The higher attrition rate the first 1-2 hours is due to the breakage of weaker particles (particles with cracks etc.) that are present in the beginning of the run, as described in 6.1. The higher attrition rate of the milled fractions is explained by fragmentation of weaker particles. In the specialization project it was concluded that incomplete sieving was part ot the explanation. Because of this, the sieving time was increased from 30 to 60 minutes. This led to a smaller amount of fines (<38 μm), as was confirmed with results from the Camsizer XT and ESEM results.

After two hours and for the rest of the run, all fractions show a linear attrition rate. As described in 6.1, this part is mainly due to abrasion which shows a linear character for the time frame of an attrition run. It could therefore be interesting to look at the linear part of the graph (from 120 min

and out). A comparison of this part for the basis and milled fractions of the three supports are shown in Figure 8.3 and Figure 8.4, respectively.

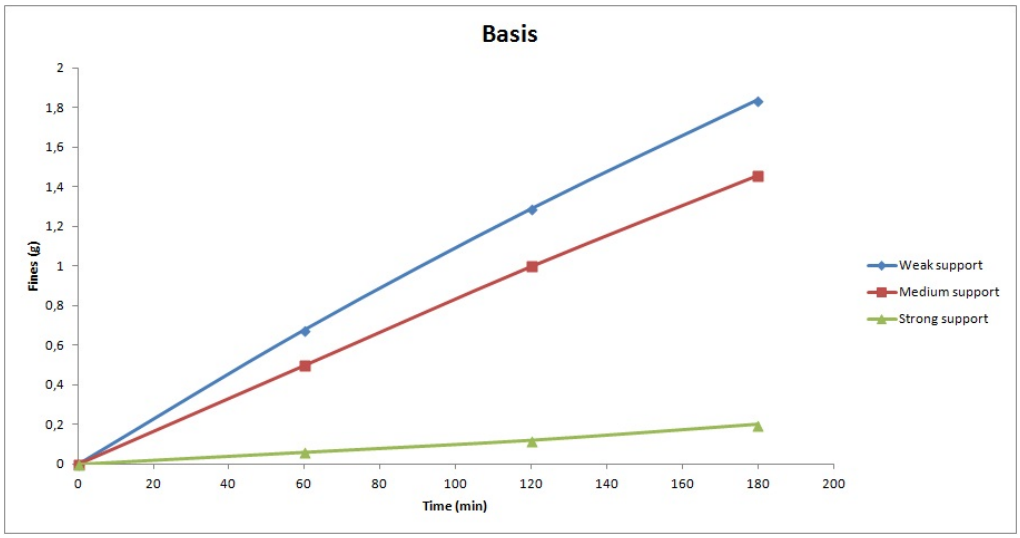

Figure 8.3: Linear part of attrition run, basis

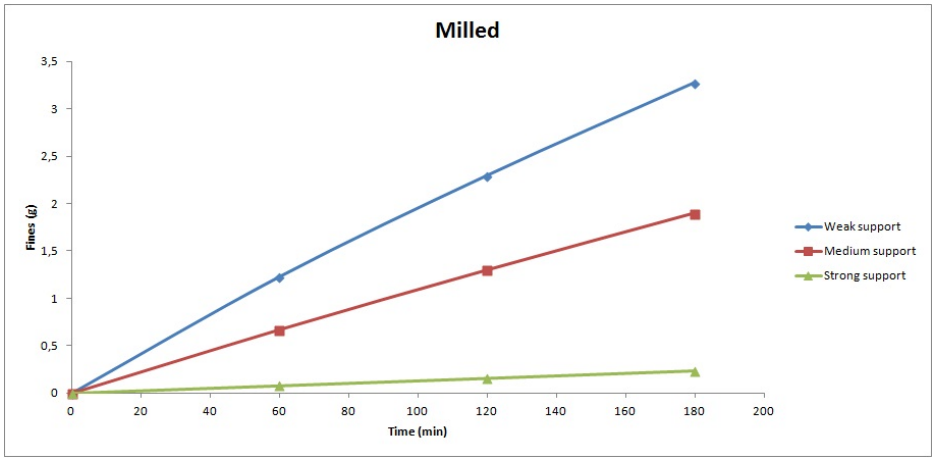

Figure 8.4: Linear part of attrition run, milled

The figures show a difference in the slope of the linear curves, with the weak support having the steepest slope and the strong support fraction having the least steep slope. These are expected results, bearing in mind the strengths of the supports. Abrasion decreases with increasing material strength. To see if there exists a correlation between the attrition and the morphology of the three different supports, the difference between attrition of the basis and milled fractions needs to be investigated. This is shown in Figure 8.5, Figure 8.6 and Figure 8.7, respectively.

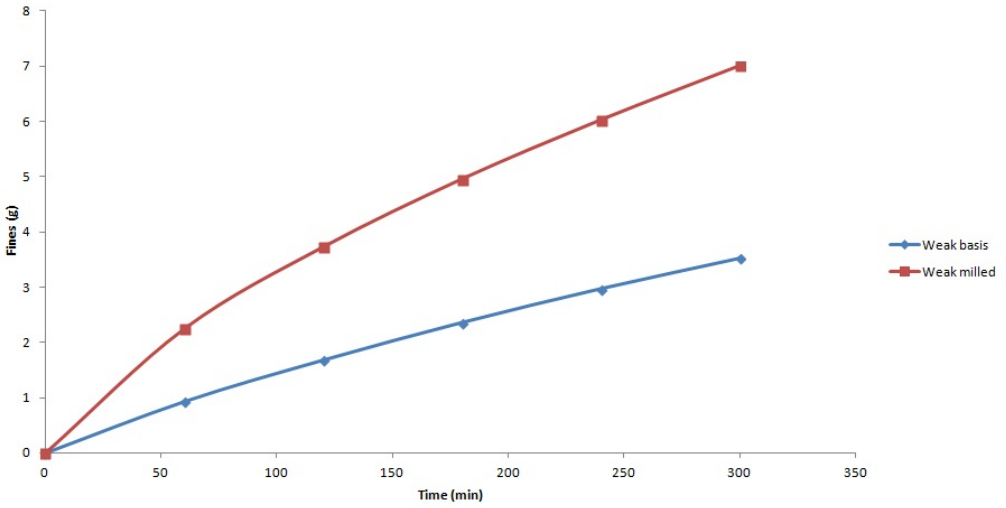

Figure 8.5: Attrition weak support

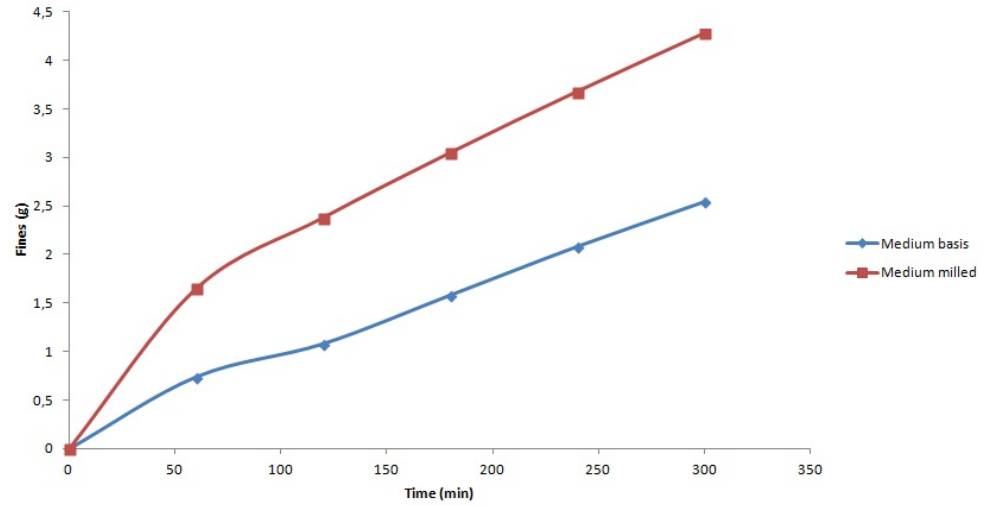

Figure 8.6: Attrition medium support

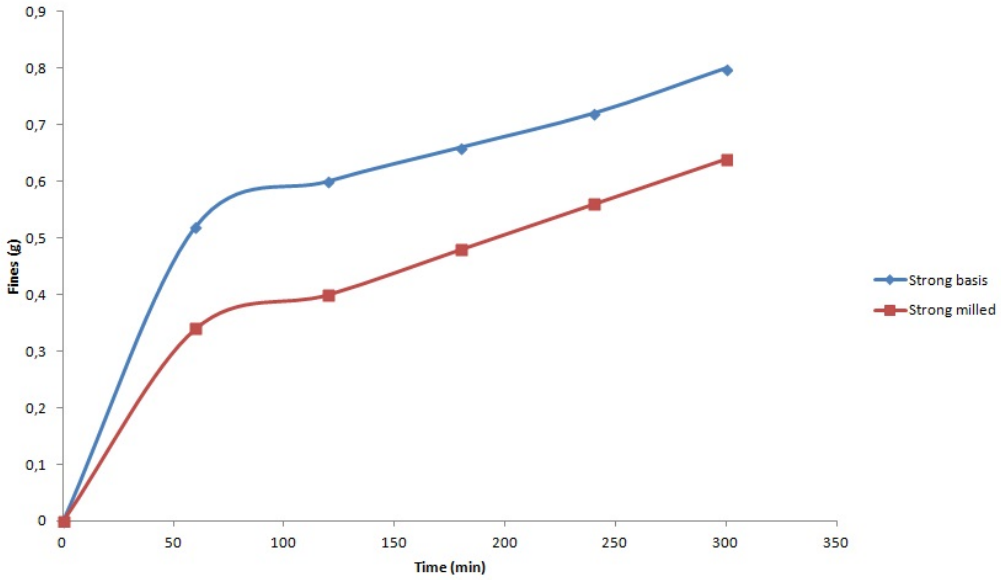

Figure 8.7: Attrition strong support

From the two first graphs it can be observed that the milled fractions have higher attrition rates. This is in accordance with the results from the specialization project where it was concluded that milling gave a less round shape, which then again led to higher attrition rates. The interesting result can be observed in Figure 8.7, where the opposite result is seen. To get an explanation for this, it is necessary to study and interpret the morphology analysis.

8.3 Camsizer XT

From the Camsizer XT software, both size and shape characteristics can be extracted. A plot of the accumulated size distribution for the three supports on volume basis is shown in Figure 8.8. Red curve is weak support, green is medium and blue is strong.

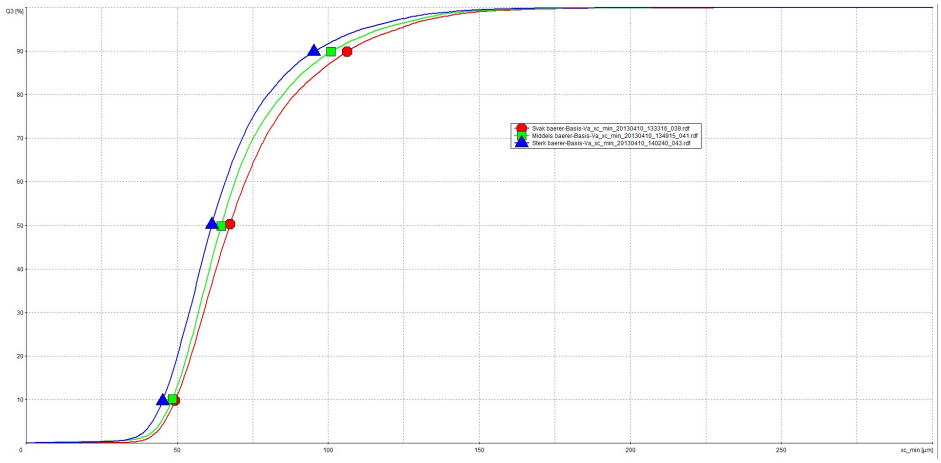

Figure 8.8: Particle size distribution, basis

In the graph, the accumulated amount on volume basis ($Q3$) is plotted as a function of the size parameter $X_{c,min}$ measured in μm. All the fractions were sieved to remove the particles smaller than 38 μm before the Camsizer analysis, because the shape of the fines is not of interest. It can be observed that the weak, unimpregnated support contains the largest particles, whereas the strong magnesium aluminate support contains the smallest. This is a result that can be seen in the context of the preparation of the material and the BET results. Calcination at high temperatures causes collapse of the pore structure of the particles, which again causes smaller particle sizes. This is shown in the BET results in Section 8.1, where a higher calcination temperature gives a smaller surface area and a smaller pore volume.

The particle size distribution of the milled fraction is shown in Figure 8.9, and the same color codes as metntioned earlier apply.

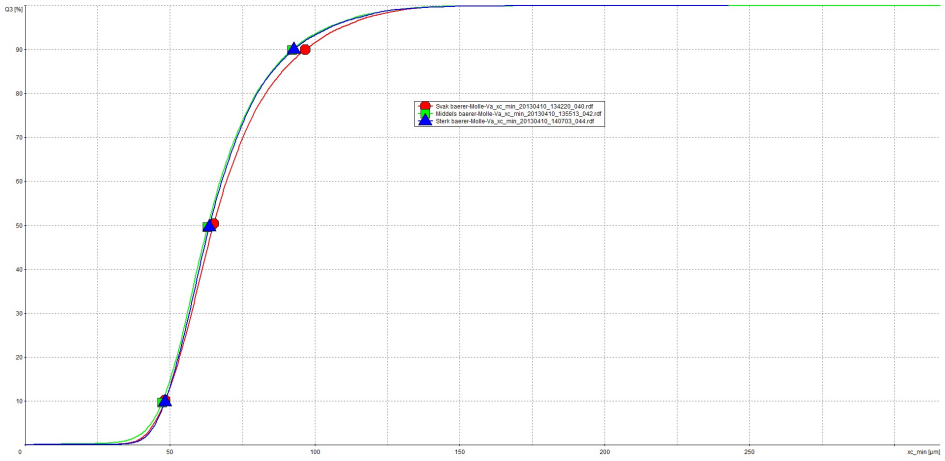

Figure 8.9: Particle size distribution, milled

The graph shows that the milling of the materials has led to a smaller size difference between the three supports. This indicates that the milling process has affected the three supports differently, which was expected. To see how the milling process affected the different supports, the software also gave shape graphs for the three supports. The attrition residual for each support was also analyzed in terms of morphology, in order to gain better knowledge of the relative differences. An overview of the graph where the accumulated amount on volume basis ($Q3$) is plotted as function of the b/l ratio described in Section 6.2 is shown in Figure 8.10 for the weak support material. Red curve is basis material, green is milled material and blue is attrition residual for the next graphs.

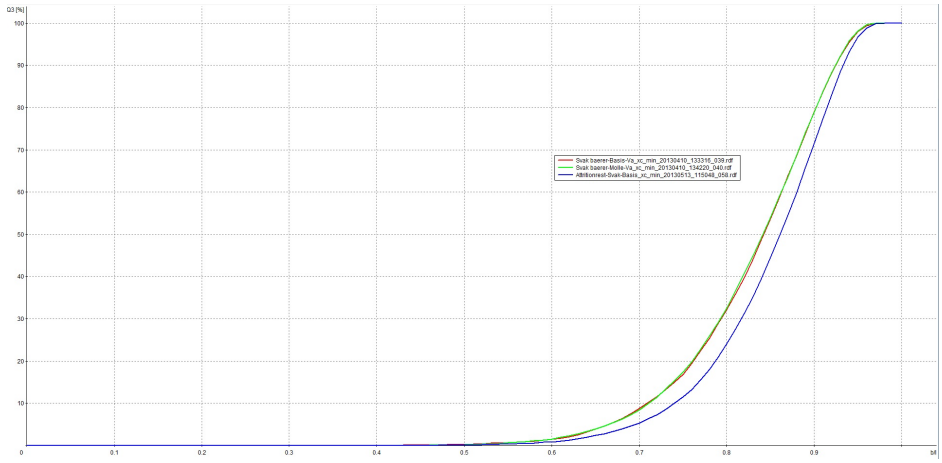

Figure 8.10: *Q3* as a function of *b/l*, weak support

A zoom of the graph at $b/l = 0{,}80$ is shown in Figure 8.11.

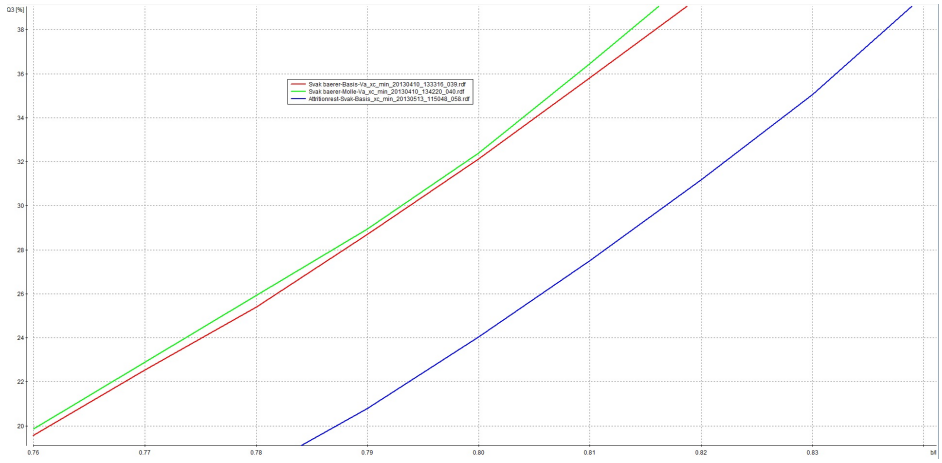

Figure 8.11: *Q3* as a function of *b/l* weak support, zoomed

From the figure it can be observed that the predicted morphology change is not observed on all points. The observed rounder particles from the attrition residual was expected in light of the results from the specialization project,

but it was not expected that the curves from the basis and milled fraction would overlap each other. With the weak material strength in mind, it was anticipated that the milling process to a large degree would change the shape of the particles. The most probable explanation to this is a too high amount of sample milled at each time. A large amount of sample (50 g) with a relative low density apparently resulted in a too high volume in the ball mill, reducing the effect of the milling.

For the medium support, a plot of $Q3$ as a function of b/l is shown in Figure 8.12.

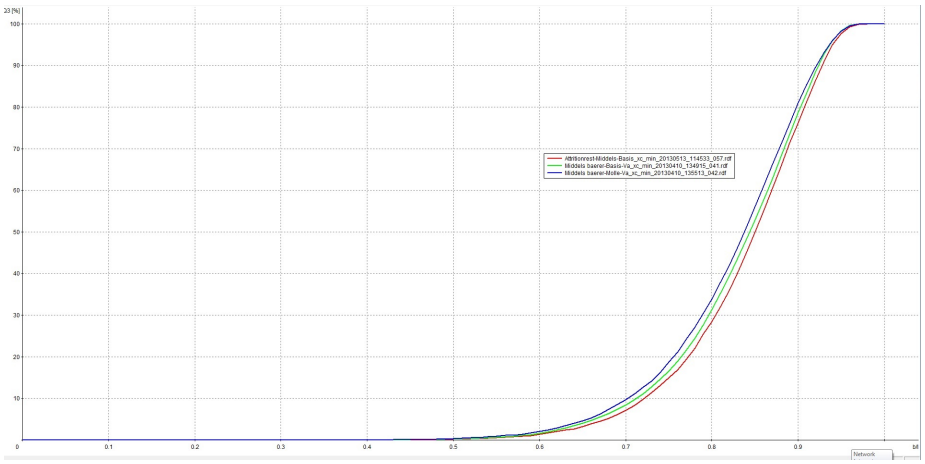

Figure 8.12: $Q3$ as a function of b/l, medium support

A zoom of the graph at $b/l = 0{,}80$ is shown in Figure 8.13.

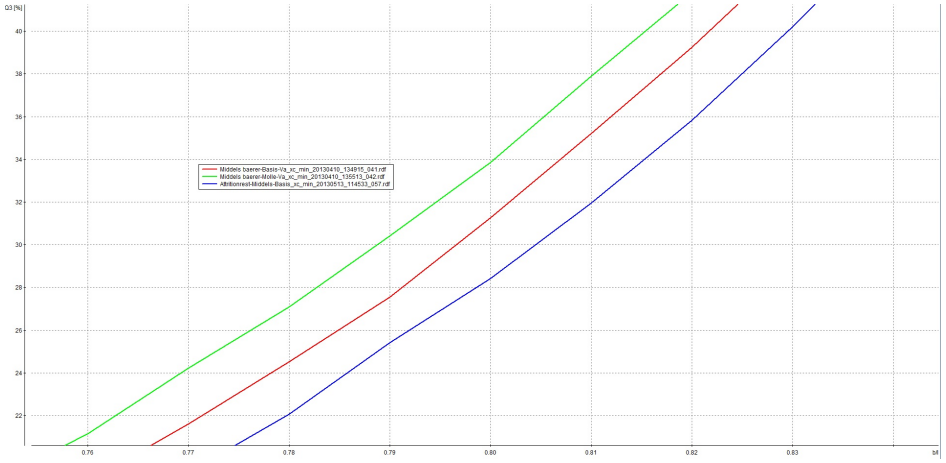

Figure 8.13: *Q3* as a function of *b/l* medium support, zoomed

In this graph, the anticipated morphology behavior is observed. The attrition residual contains more rounded particles, whereas the milled fraction has a less round shape than the basis material. Although the differences go in the right direction, the magnitude of the change is not as big as expected. The difference in morphology between the basis and the milled material is less here than from the identical analysis performed in the specialization project. The reasoning behind is likely to be equal of that of the weak support material.

For the strong support, a plot of *Q3* as a function of *b/l* is shown in Figure 8.14.

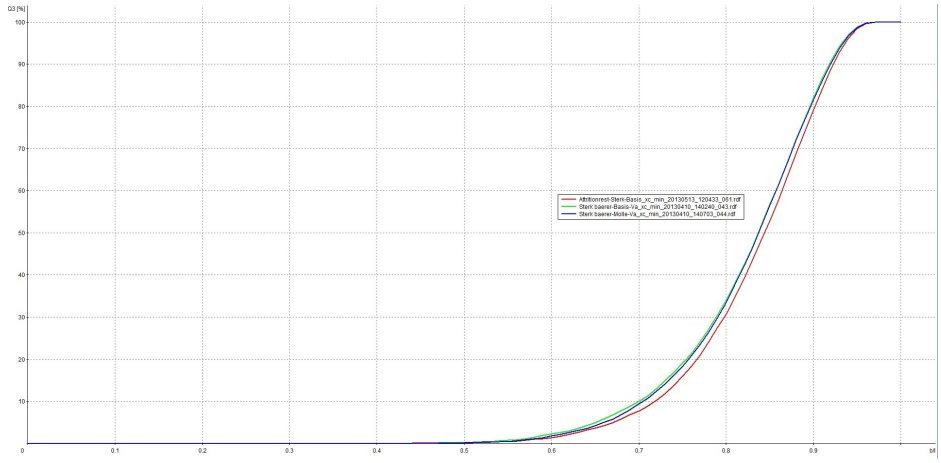

Figure 8.14: *Q3* as a function of b/l, strong support

A zoom of the graph at $b/l = 0{,}80$ is shown in Figure 8.15.

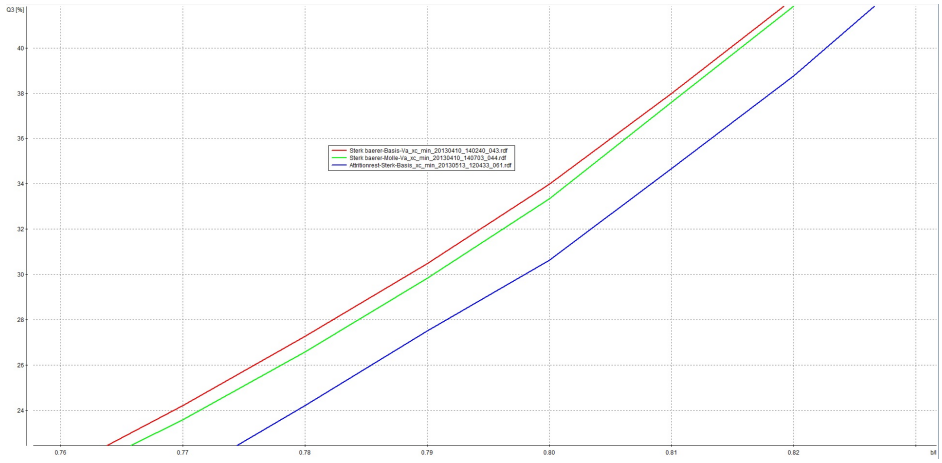

Figure 8.15: *Q3* as a function of b/l strong support, zoomed

Here it is observed that the curves for the basis material and the milled fraction overlap, and that the attrition residual is rounder to a certain degree. This, together with the results from the attrition experiment and the

low amount of fines produced in the milling process, shows that the strong support has an excellent material strength and is very resistant towards fragmentation in the ball mill.

Samples of the attrition residual were taken out before the run, after 1 hour, 3 hours and 5 hours for the weak support to observe how the particle morphology change over time. This is seen in Figure 8.16. Red curve is 0 hour, green is 1 hour, blue is 3 hours and purple is 5 hours.

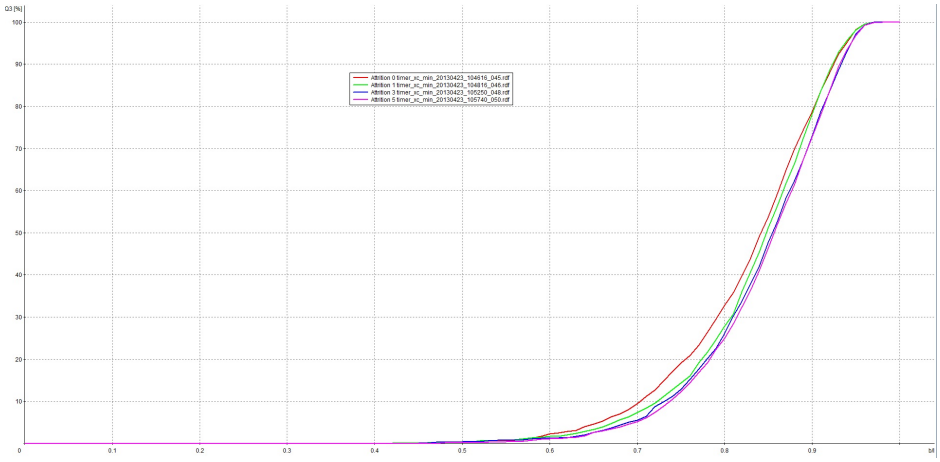

Figure 8.16: *Q3* as a function of b/l attrition 1-3-5 hours

A zoom of the graph at $b/l = 0{,}80$ is shown in Figure 8.17.

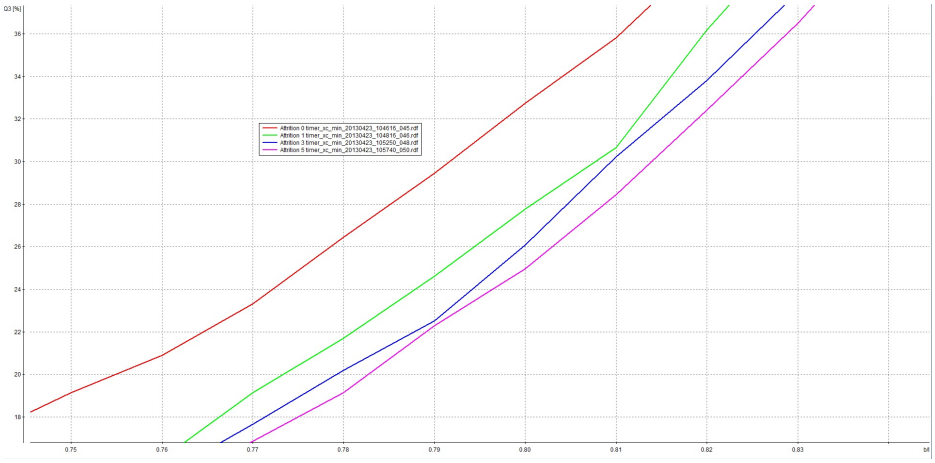

Figure 8.17: *Q3* as a function of *b/l* attrition 1-3-5 hours, zoomed

From these graphs it can be observed a gradual rounding of the alumina particles over time, and the largest change in particle shape is seen from the start to the 1 hour mark. This confirms the effects of the attrition rig on the support particles, and shows that the corners and kinks of the particles are gradually grinded off. Exposure to the jet stream in the rig for a longer period of time would probably make the particles even rounder. The curves are not as smooth as they should be because of a small amount of sample available. This leads to a degree of uncertainty associated to the measurements, but the general trends can still be observed.

Another feature of the Camsizer *XT* software is that it calculates the mean value of the shape paramter. These values are listed in Table 8.3.

Table 8.3: Shape parameters

Material	**Mean value b/l**
Weak basis	0,834
Weak milled	0,834
Weak attrition	0,852
Medium basis	0,835
Medium milled	0,829
Medium attrition	0,841
Strong basis	0,828
Strong milled	0,830
Strong attrition	0,836
Attrition 0 hours	0,830
Attrition 1 hours	0,837
Attrition 3 hours	0,844
Attrition 5 hours	0,847

From the table it is confirmed that the shape parameters of the different fractions are quite similar. This confirms that the magnesium modified alumina particles are very robust, and that the breakage mechanisms are independent of particle shape. It is also a confirmation that the morphology altering process (the ball mill) did not produce the desired results. In the next sub chapter it is discussed whether a correlation exists between the attrition resistance and the morphology of the particles for the three supports, and between morphology and catalytic activity.

8.4 ESEM images

Images of the basis and milled fractions of the three supports were taken at different magnifications for comparison purposes. This is depicted in Figure 8.18 and 8.19 for the weak support.

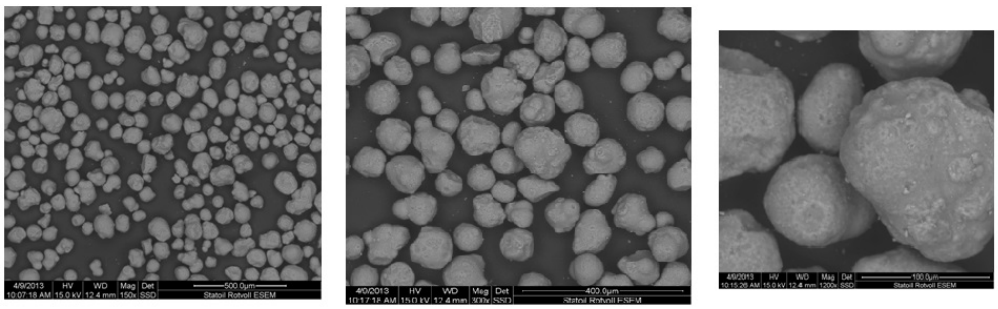

Figure 8.18: ESEM weak support, basis

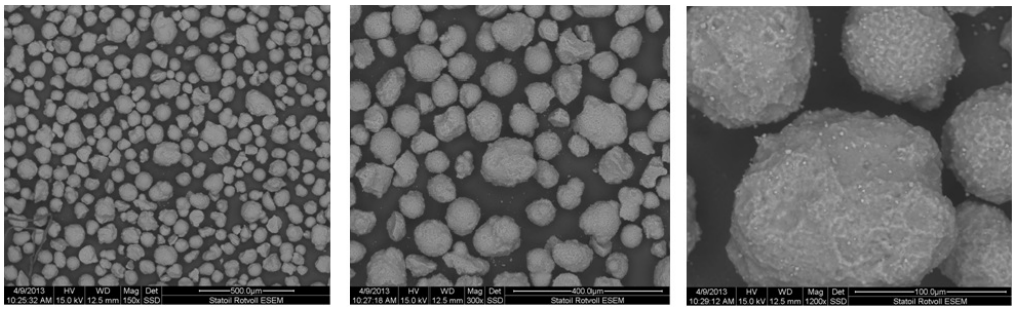

Figure 8.19: ESEM weak support, milled

From the images it can be seen that the shape of the particles is spherical, but with defects and irregularities on some of them. The ESEM images confirm the results from the Camsizer analysis, namely that the shape of the weak support material has not been altered by the milling process. This underlines the suspicion that the milling process did not act as expected, probably

because of the amount of material milled at once. Unimpregnated alumina, which is not calcined at high temperatures, should have its morphology more altered by such a process.
ESEM images for the medium support are depicted in Figure 8.20 and 8.21.

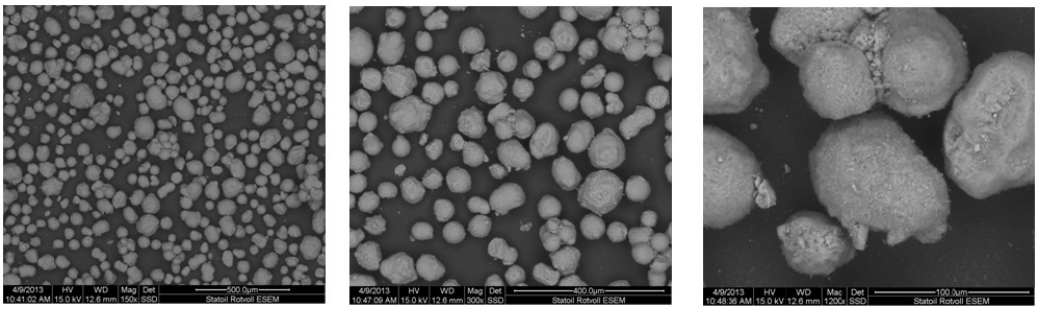

Figure 8.20: ESEM medium support, basis

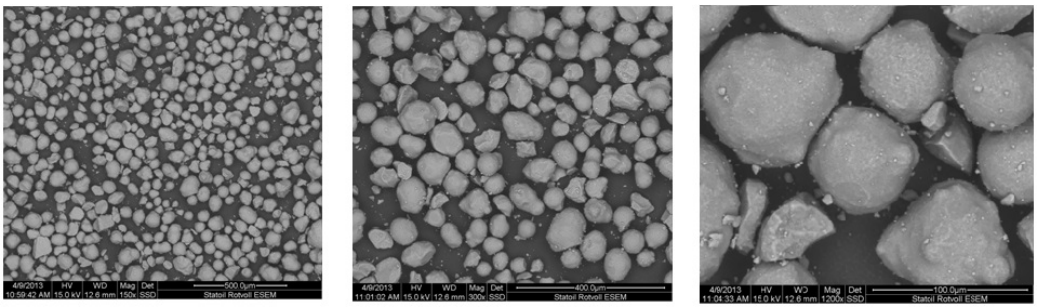

Figure 8.21: ESEM medium support, milled

The particles in the pictures of the basis material are quite similar to the particles of the weak support. The largest difference is the presence of agglomerates, which probably is due to excess of liquid from the impregnation process. For the medium support, a difference between the basis and the

milled fraction can be observed. Some of the particles have clearly been fragmented and therefore had their shape altered. The difference is still not as large as observed in the specialization project, as discussed earlier.
ESEM images for the strong support are depicted in Figure 8.22 and 8.23.

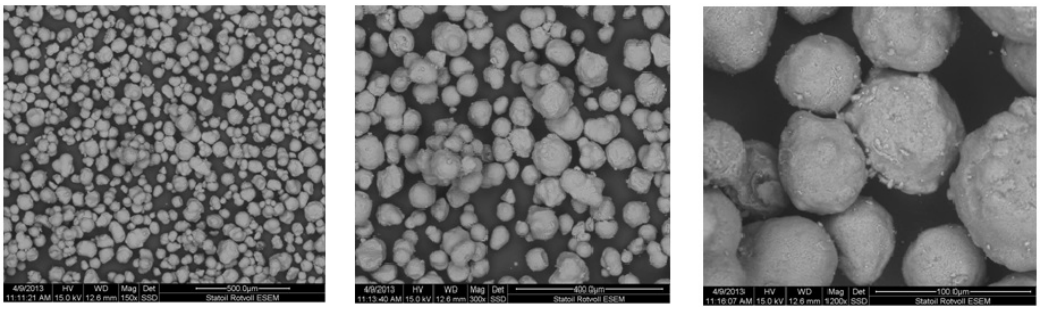

Figure 8.22: ESEM strong support, basis

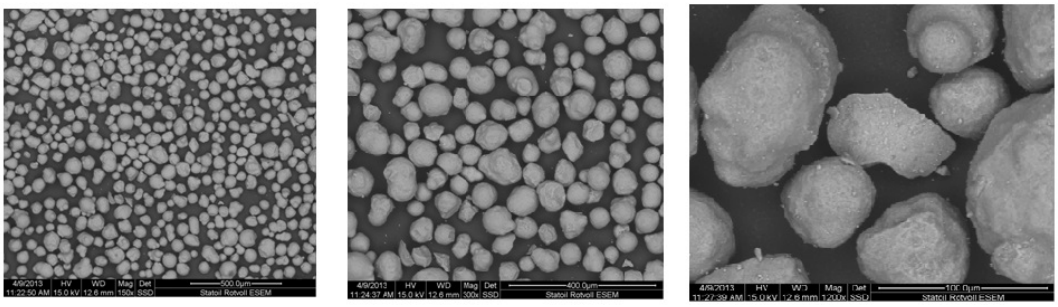

Figure 8.23: ESEM strong support, milled

These images show some of the same information as the pictures of the medium strength support, regarding the presence of agglomerates. The biggest difference is the smaller amount of fragmented particles present in the milled fraction, indicating a much stronger material. This corresponds well with the results from the Camsizer analysis, where the shape curves of

the basis and the milled fraction overlap.

ESEM images were also taken for the samples of the attrition residual of the weak support, taken at 1, 3 and 5 hours. This is shown in Figure 8.24.

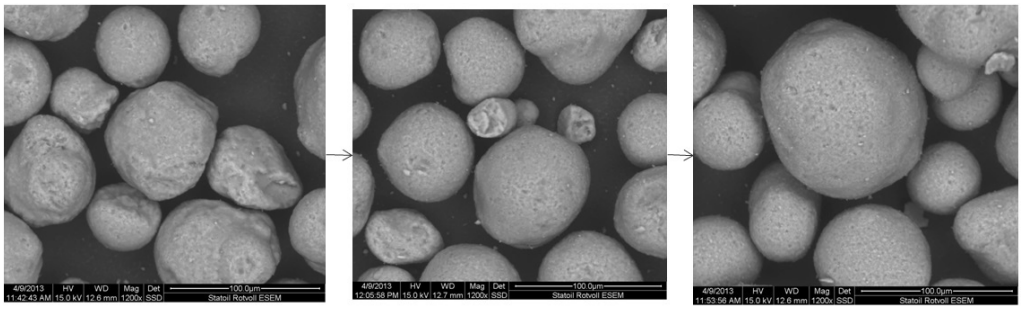

Figure 8.24: ESEM attrition residual 1-3-5 hours

The ESEM images confirm the results from the Camsizer where a gradually rounding could be observed. This can be observed in the image above, especially between the fractions from after 1 hour and after 3 hours.

8.5 Chemisorption

The results of the measurements described in Chapter 7.7 are listed in Table 8.4.

Table 8.4: Chemisorption results

Support	**Dispersion**(%)	**Metallic surface area**(m^2/g_{sample})
Weak basis	10,5	8,5
Weak milled	10,3	8,4
Medium basis	8,5	6,9
Medium milled	9,1	7,4

From the table it can be seen that the weak, unimpregnated alumina particles give a higher dispersion of cobalt than the impregnated magnesium aluminate calcined at 950° C. This is related to the difference in available suraface area, which is given in 8.1. Correlating these results with the morphology results is not straightforward because of the relative small differences both in dispersion and morphology. For the weak support particles the morphology was identical, and the dispersion is also very similar. The medium support particles have more uneven particles in the milled fraction than the basis, and the dispersion of cobalt on the milled fraction is a bit higher as well. It is well known that small particles have higher dispersion because they expose a larger amount of the surface as corners and edges which are more accessible for adsorption [11]. This is in accordance with the chemisorption results, where the most uneven particles have the highest dispersion values.

The cobalt particle size was calculated for the four catalysts. Calculations are shown in A.5, and the results are listed below in Table 8.5.

Table 8.5: Cobalt particle size calculated from dispersion values

Support	**Cobalt particle size(nm)**
Weak basis	9,2
Weak milled	9,3
Medium basis	11,3
Medium milled	10,6

8.6 Activity results

Three of the prepared catalysts were tested for FT activity and selectivity in a fixed bed reactor. The catalyst prepared from the weak support did show a higher conversion than the magnesium aluminate based catalysts. Therefore, the conversion was tuned down by adjusting the space velocity in order to obtain similiar conversion values for comparing the selectivity towards (C_{5+}). A plot of the CO-conversion and (C_{5+}) selectivity as a function of time on stream (TOS) is given in Figure 8.25.

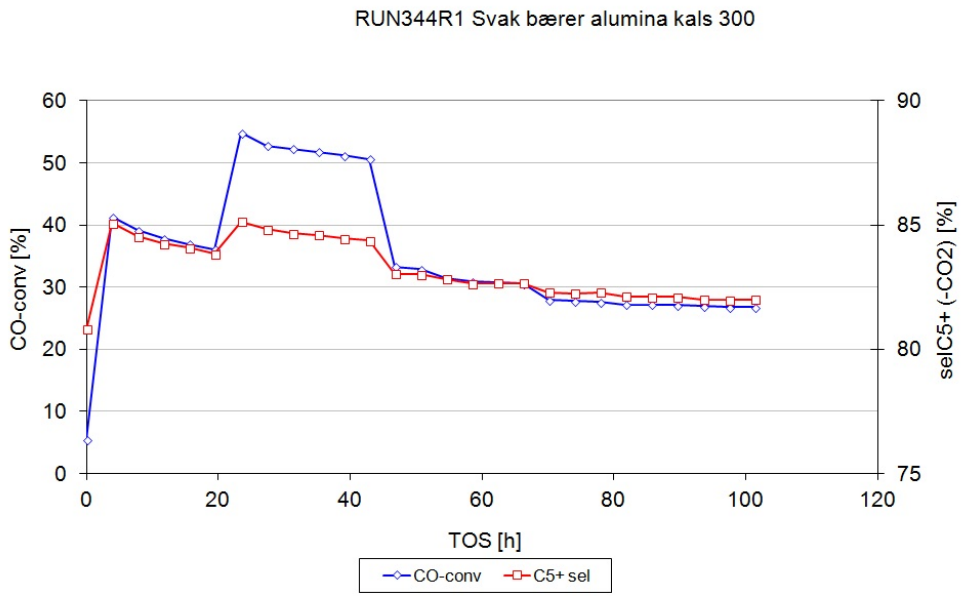

Figure 8.25: CO-conversion and (C_{5+}) selectivity as a function of TOS, weak support

From the graph it can be observed that the CO-conversion raises above 50 %, before it is tuned down to around 30 %. The reason for this can be seen in Figure 8.26 and 8.27, where plots for the medium basis and milled catalyst are shown.

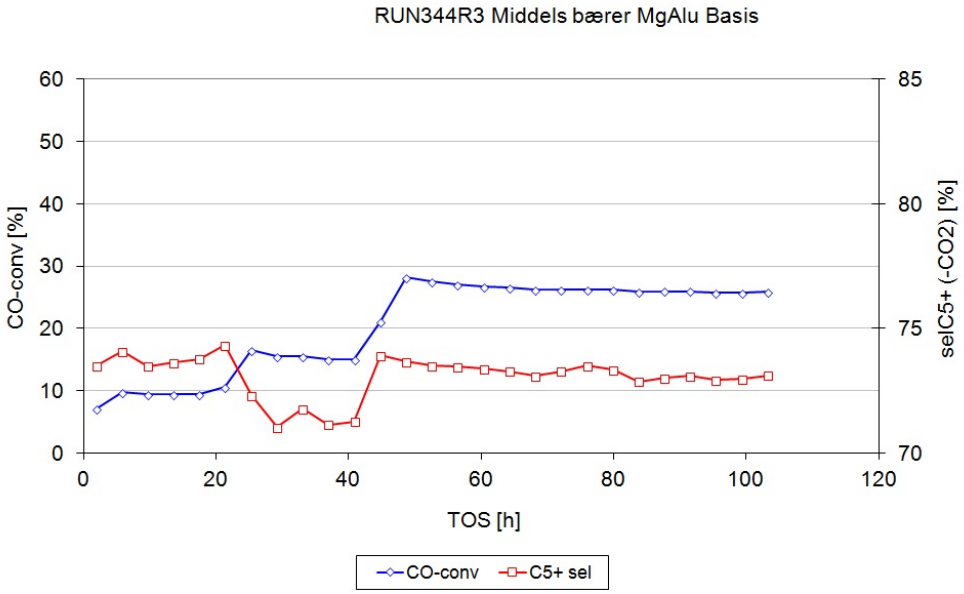

Figure 8.26: CO-conversion and (C_{5+}) selectivity as a function of TOS, medium basis

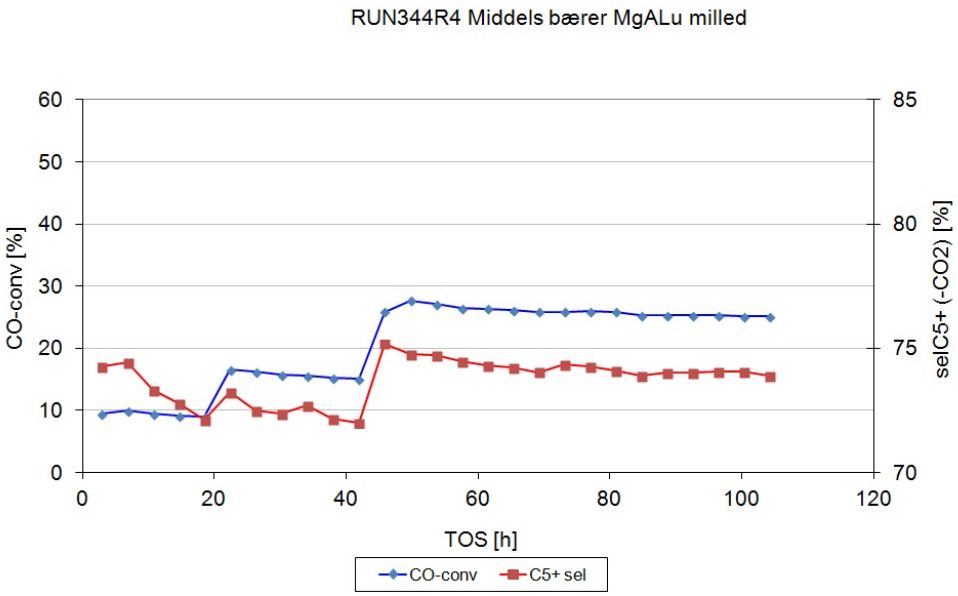

Figure 8.27: CO-conversion and (C_{5+}) selectivity as a function of TOS, medium milled

The CO-conversion for these two catalysts never reach higher than around 30 %, so in order to compare selectivities (selectivity is a function of conversion) the catalyst with high conversion had to have its space velocity reduced. It is noteworthy to notice the difference in selectivity between the catalyst based on the weak support and the catalysts based on the medium supports. For the weak support, the (C_{5+}) selectivity is around 82 %, whereas the medium support catalysts have selectivities around 73-74 % after 100 hours on stream. The selectivity towards long-chained hydrocarbons is dependent on process conditions such as temperature and pressure, and the nature of the catalyst. Cobalt produces long-chained hydrocarbons, so the previously reported small difference in cobalt dispersion could play a role. The difference is, however, too small to account for the relative big difference in the (C_{5+}) selectivity. For the medium support catalysts, the difference between the basis and milled fratcion is small, with the selectivity for the milled material being about 1 % higher. This difference can be accounted for with the

difference in cobalt dispersion reported earlier.

Another important parameter is the catalytic activity. The rate of different length hydrocarbon chains is plotted as a function of TOS for the weak support catalyst, as depicted in Figure 8.28.

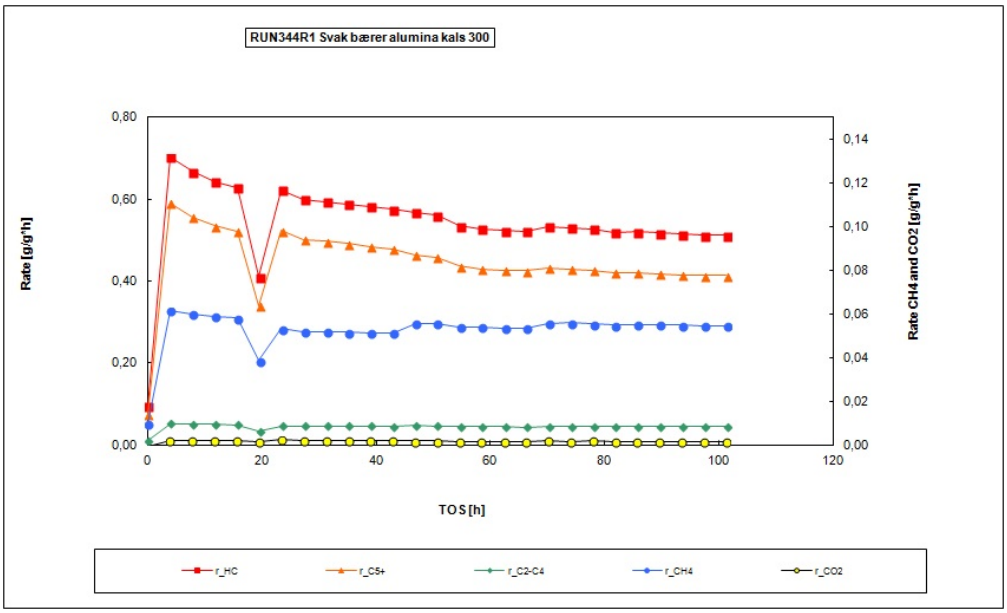

Figure 8.28: Reaction rate as a function of TOS, weak support

The reaction rate for the long-chained hydrocarbons is around 0,4 g CO per g catalyst and hour, after 100 hours on stream. Converted to TOF, this gives around 0,02 s^{-1}. Calculations are shown in A.6. Similiar plots are given for medium basis and medium milled catalyst in Figure 8.29 and 8.30.

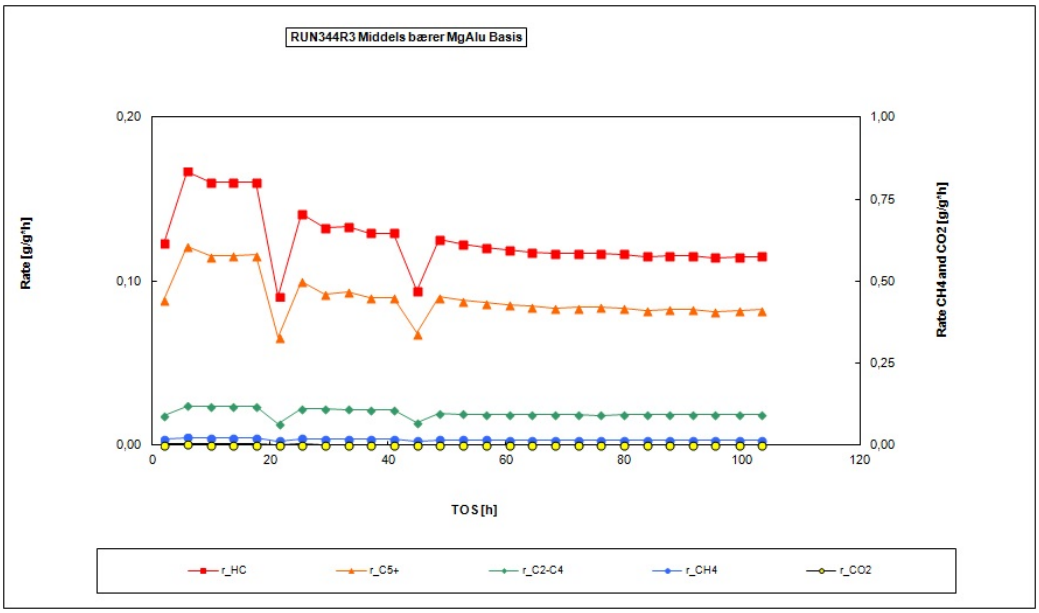

Figure 8.29: Reaction rate as a function of TOS, medium basis

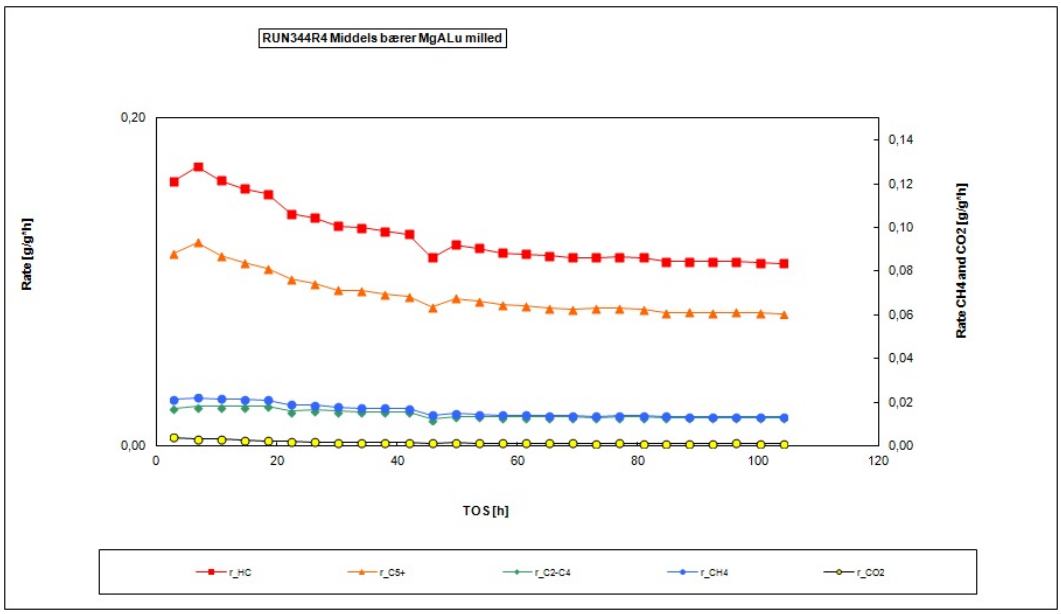

Figure 8.30: Reaction rate as a function of TOS, medium milled

The reaction rates for long-chained hydrocarbons for the two medium strength catalysts are around 0,1 g CO per g catalyst and hour (0,005 s^{-1}, see A.6), and is only 1/4 of the activity of the weak support catalyst. This is partly due to the lower dispersion of cobalt, and partly due to the magnesium acting as a poison for the FT synthesis as reported in litterature [6]. The graphs show a small difference between the medium basis catalyst and the medium milled catalyst, with the milled fraction having a slightly higher activity. This is probably due to the higher cobalt dispersion, as mentioned earlier.

9 Conclusion and recommendation for further work

It has been difficult to find a correlation between particle morphology and particle attrition for three different alumina based catalyst supports for the Fischer-Tropsch synthesis. The chosen method of morphology altering, a ball mill, turned out to give very small differences in the particle shape. A one step incipient wetness impregnation of 10 wt.% Mg on γ-alumina calcined at 1050° C yielded a very strong material with good attrition resistance, and with small possibilities for altering the morphology. The two other supports, magnesium aluminate calcined at 1050° C and unimpregnated alumina, also had a small effect of the milling process. This was explained by a too large amount of sample fed to the ball mill each time (50 g), which probably had the biggest effect on the weak support because of its lower density. The small differences in particle shape observed by the particle analyzer (Camsizer XT) were confirmed by the images from the electron microscope (ESEM).

The attrition ranking of the different fractions, from highest to lowest attrition rate, is shown below:

Weak milled > Weak basis > Medium milled > Medium basis > Strong basis > Strong milled

The milled fraction had a higher attrition rate than its basis counterpart in the weak and medium strength supports, but the opposite was observed for the strong support material. Milling of the strong support actually led to slightly more round particles, which corresponds well with the results from the specialization project that showed that rounder particles resulted in a lower attrition rate. The general trend from the results in the specialization project seems to hold, although the differences in particle shape were much smaller than hoped.

A correlation between particle morphology and catalytic activity has also been difficult to determine. Cobalt-based Fischer-Tropsch catalysts with 12 wt.% Co and 0,5 wt.% Re were prepared using a one step incipient wetness impregnation, for the weak and medium basis and milled support fractions. A small correlation between particle shape and cobalt dispersion was found, namely that decreased roundness yielded increased dispersion values. This difference in cobalt dispersion yielded a small difference in catalytic activity and selectivity for the basis and milled fraction of catalyst based on the medium strength support. The differences are too small to conclude with a correlation.

The most important recommendation for further work would be to examine the possibilities for changing the morphology of catalyst support particles more thoroughly. To obtain larger variations in particle shape it would be advisable to use smaller amounts at a time in the ball mill. Even greater variations can be obtained with a support material with inferior mechanical strength, like for instance amorphous silica based supports. If a significant correlation between particle morphology and catalytic activity could be found, it would be interesting to investigate the profitability of pre-treating the catalyst support in order to change the particle shape.

10 List of symbols

Table 10.1: Symbol list

Symbol	Unit	Description
α	-	Phase of alumina
δ	-	Phase of alumina
γ	-	Phase of alumina
θ	-	Phase of alumina
θ	rad	Contact angle
a	-	Fraction of cobalt
b	-	Fraction of rhenium
b/l	-	Width/length ratio
C	-	BET constant
K	-	Rate constants ratio
M_A	g/mol	Molar mass Co
M_{A-salt}	g/mol	Molar mass Co salt
M_B	g/mol	Molar mass Re
M_{B-acid}	g/mol	Molar mass Re acid
M_{Mg}	g/mol	Molar mass Mg
$M_{\mathrm{Mg(NO_3)_2 \cdot 6\,H_2O}}$	g/mol	Molar mass Mg salt
m_f	g	Weight fines
m_{H_2O}	g	Weight water
$m_{H_2O_{abs}}$	g	Weight absorbed water
m_s	g	Weight sample
m_{supp}	g	Weight support
N_s	-	Number of metal surface atoms
N_t	-	Total number of metal atoms
p	Pa	Pressure
p_0	Pa	Saturation pressure
$Q3$	%	Accumulated amount on volume basis

Continued on next page

Table 10.1 – *Continued from previous page*

Symbol	**Unit**	**Description**
R	J/K,mol	Gas constant
r	nm	Pore radius
r_{CO}	mol CO/(g cat*h)	Reaction rate
S	N/m	Surface tension
s	-	Fraction of alumina
T	K	Temperature
TOF	s^{-1}	Turnover frequency
V	m^3	Adsorbed volume
V	m^3/mol	Molar volume
X_{area}	μm	Size parameter Camsizer
$X_{c,min}$	μm	Size parameter Camsizer
$X_{Fe,max}$	μm	Size parameter Camsizer
x	%	Weight fraction of metal

11 List of abbreviations

Abbreviation	Description
ASA	Allmennaksjeselskap
ATR	Autothermal reforming
BET	Brunauer, Emmet and Teller
ESD	Environmental Secondary Detector
ESEM	Environmental Scanning Electron Microscope
FCC	Face-centered cubic
FT	Fischer-Tropsch
FTS	Fischer-Tropsch synthesis
GTL	Gas-to-liquids
h	Hour
MFC	Mass Flow Controller
Min	Minutes
NTNU	Norges teknisk-naturvitenskapelige universitet
PLA	Pressure Limiting Apperature
PSD	Particle size distribution
R&D	Research and development
SEM	Scanning Electron Microscope
TOF	Turnover frequency
TOS	Time on stream
WGS	Water-gas-shift
Wt.%	Weight percentage

References

[1] BP, "BP Energy Outlook 2030," January 2013.

[2] B. White, "Schematic of the GTL process," June 2012. http://www.arcticgas.gov/can-gas-liquids-technology-get-traction.

[3] E. Iglesia, "Design, synthesis and use of cobalt-based Fischer-Tropsch synthesis catalysts," *Applied Catalysis*, vol. 161, pp. 59–78, 1997.

[4] M. E. Dry, "The Fischer-Tropsch process: 1950-2000," *Catalysis Today*, vol. 71, pp. 227–241, 2002.

[5] D. Wu, J. Zhou, and Y. Li, "Mechanical Strength of Solid Catalysts: Recent Developments and Future Prospects," *AiChE Journal*, vol. 53, pp. 2618–2629, 2007.

[6] E. Rytter, S. Eri, D. Schanke, H. Wigum, T. Skagseth, Øyvind Borg, and E. Bergene, "Development of an Attrition Resistant Fischer-Tropsch Catalyst for Slurry Operation," *Topics in Catalysis*, vol. 54, pp. 801–810, 2011.

[7] J. Gwyn, "On the Particle Size Distribution Function and the Attrition of Cracking Catalysts," *Journal of A.I.Ch.E*, vol. 15, p. 35, 1969.

[8] RetschTechnologies, "Camsizer XT brochure," November 2012. http://www.retsch-technology.com/rt/products/dynamic-image-analysis/camsizer-xt/function-features/.

[9] E. A. Blekkan, "Presentation about deactivation given in module TKP2," October 2012.

[10] K. Kimseng and M. Meissel, "Short overview about the ESEM: Environmental Scanning Electron Microscopy," February 2001. http://www.calce.umd.edu/TSFA/ESEM.pdf.

[11] M. Rønning, "Presentation about adsorption given in subject TKP4155," September 2011.

[12] DirectIndustry, "Laboratory ball mill product information," May 2013. http://www.directindustry.com/prod/spex-certiprep-ltd/laboratory-ball-mills-65554-450832.html.

[13] F. Scientific, "Methylacrylate balls product information," May 2013. http://www.fishersci.com/ecomm/servlet/itemdetail?productId=2174149&storeId=10652&langId=-1#.

[14] U. of Cambridge, "Environmental Scanning Electron Microscopy," November 2012. http://www.phy.cam.ac.uk/research/bss/esem.php.

[15] I. Chorkendorff and J. Niemantsverdriet, *Concepts of Modern Catalysis and Kinetics*. Wiley-VCH, 2 ed., 2007.

[16] T. Ukeblad, "Slik produseres renere diesel," August 2012. http://www.tu.no/industri/2012/08/27/slik-produseres-renere-diesel.

[17] H. Schulz, "Short history and present trends of Fischer-Tropsch synthesis," *Applied Catalysis*, vol. 186, pp. 3–12, 1999.

[18] N. E. Tsakoumis, M. Rønning, Øyvind Borg, E. Rytter, and A. Holmen, "Deactivation of cobalt based Fischer-Tropsch catalysts: A review," *Catalysis Today*, vol. 154, pp. 162–182, 2010.

[19] B. M. H. Board, *Particle Attrition, State-of-the-Art Review*, vol. 5 of *Series on Bulk Materials Handling*. Trans Tech Publications, 1987.

[20] R. Zhao, J. G. Jr, and R. Oukaci, "Attrition assessment for slurry bubble column reactor catalysts," *Applied Catalysis*, vol. 189, pp. 99–116, 1999.

[21] RetschTechnologies, "Camsizer XT operating manual," November 2012.

[22] J. T. Richardson, *Principles of Catalyst Development.* Plenum Press, 1 ed., 1989.

[23] S. Brunauer, P. Emmett, and E. Teller, "Adsorption of Gases in Multimolecular Layers," *Journal of the American Chemical Society*, vol. 60, pp. 309–319, 1938.

[24] A. Holmen, *Heterogen katalyse.* Institutt for kjemisk prosessteknologi, NTNU, 1 ed., 1996.

[25] R. D. Jones and C. H. Bartholomew, "Improved Flow Technique for Measurement of Hydrogen Chemisorption on Metal Catalysts," *Applied Catalysis*, vol. 39, pp. 77–88, 1988.

[26] D. V. N. Prasad and J. Theuerkauf, "Effect of Grinding Media Size And Chamber Length on Grinding in a Spex Mixer Mill," *Chemical Engineering and Technology*, vol. 32, pp. 1102–1106, 2009.

[27] G. Aylward and T. Findlay, *SI Chemical Data.* John Wiley, 6 ed., 2008.

[28] A. E. Karlsen, *Synthesis and Characterisation of Co-based Fischer-Tropsch Catalysts and Supports, using hydrothermal and chemical attrition Method: The magnesium moderation Effect.* NTNU, 1 ed., 2011.

A Calculations

In this appendix all the calculations regarding the experiments can be found. Not all calculations are shown in detail.

A.1 Water absorptivity

To calculate the amount of water which is needed for the incipient wetness impregnation, it is first needed to obtain the water absorptivity for the material being impregnated. This is done by weighing out a small amount of support and dropwise adding water until the point where all the pores are filled. The point of total capillary condensation is observed by excess of liquid after stirring. The water absorptivity is recognized as the ratio between amount of water needed and the weight of the support. For the commercial alumina used to impregnate magnesium, the value was given to be 1,25. For the magnesium aluminate, the water absorptivity was done manually. The mass of the support and the mass of water needed to reach total capillary condensation were measured, and the water absorptivity could then be calculated by:

$$Abs = (\frac{m_{H_2O_{abs}}}{m_{supp}}) = \frac{6,90}{7,65} = 0,90 \tag{A.1}$$

where m_{supp} is the amount of support. The amount of water can then be calculated by:

$$m_{H_2O} = Abs * m_s \tag{A.2}$$

where m_s is the weight of the sample.

A.2 Amount of Mg salt for impregnation

To find the amount of Magnesium salt ($Mg(NO_3)_2 \cdot 6\,H_2O$) needed for impregnation, it is necessary to calculate the ratio between Mg salt and support. In the experiments performed, 10 weight percent of Mg was desired. The molar masses of the compounds are taken from [27]. The calculations are shown below:

$$\frac{M_{Mg(NO_3)_2 \cdot 6\,H_2O}}{M_{Mg}} = \frac{256,4}{24,3} = 10,55 \tag{A.3}$$

Then the ratio can be calculated:

$$\frac{m_{Mg}}{m_{alumina}} * \frac{M_{Mg(NO_3)_2 \cdot 6\,H_2O}}{M_{Mg}} = \frac{10}{90} * 10,55 = 1,17 \tag{A.4}$$

A.3 Amount of Co and Re for catalyst impregnation

To find the amount of cobalt salt ($Co(NO_3)_2 \cdot 6\,H_2O$) and rhenium acid ($HReO_4$) needed for impregnation, it is necessary to calculate the ratio between salt/acid and support. In the experiments performed, 12 weight percent of Co and 0,5 weight percent of Re was desired. The molar masses of the compounds are taken from [27]. The calculations are shown below:

$$m_A = \frac{a * m_s}{s} * \frac{M_A}{M_{A-salt}} = \frac{0,12 * m_s}{0,875} * \frac{58,93}{291,02} = 0,68g\frac{Co - salt}{support} \tag{A.5}$$

where a is the fraction of cobalt and s is the fraction of alumina.

$$m_B = \frac{b * m_s}{s} * \frac{M_B}{M_{B-acid}} = \frac{0,005 * m_s}{0,875} * \frac{186,2}{251,2} = 0,01g\frac{Re - acid}{support} \quad \text{(A.6)}$$

where b is the fraction of rhenium and s is the fraction of alumina.

A.4 Attrition

The attrition values are given as percentage of fines after 5 hours. For instance, the attrition of the basis of the weak support material is easily calculated by:

$$Attrition = (\frac{m_f}{m_s}) * 100\% = (\frac{3,52}{50,84}) * 100\% = 6,92\% \quad \text{(A.7)}$$

Equal calculations were performed for the other attrition runs.

A.5 Cobalt particle size

The average cobalt particle size can be calculated from 6.7. Calculation for the basis of the weak support is shown below.

$$d = \frac{96,2}{10,5} = 9,2nm \quad \text{(A.8)}$$

A.6 Catalytic activity

The catalytic activity can be expressed by turnover frequency (TOF). TOF can be calculated by [28]:

$$TOF = \frac{-r_{CO} * M}{3600 * x * D} \tag{A.9}$$

where $-r_{CO}$ is the reaction rate in mol CO per g catalyst and hour, M is molar mass of cobalt, x is weight fraction cobalt and D is the dispersion. The reaction rate has to be converted from g/g*h to mol/g*h. The calculations for the three catalysts are shown below, in the order weak basis - medium basis - medium milled :

$$TOF = \frac{-r_{CO} * M}{3600 * x * D} = \frac{(\frac{0,4}{28,01}) * 58,93}{3600 * 0,12 * 0,105} = 0,019 s^{-1} \tag{A.10}$$

$$TOF = \frac{-r_{CO} * M}{3600 * x * D} = \frac{(\frac{0,09}{28,01}) * 58,93}{3600 * 0,12 * 0,091} = 0,005 s^{-1} \tag{A.11}$$

$$TOF = \frac{-r_{CO} * M}{3600 * x * D} = \frac{(\frac{0,11}{28,01}) * 58,93}{3600 * 0,12 * 0,085} = 0,006 s^{-1} \tag{A.12}$$

B Raw data

B.1 Attrition data

	A	B	C	D	E	F	G	H	I	J	K	L
1	**Mg_Aluminat-Basis-950C**				**Mg_Aluminat-Mølle-950C**				**Alumina-Basis**			
2		Tid (min):	Fines (gram)	Diff(gram):		Tid (min):	Fines (gram):	Diff(gram):		Tid (min):	Fines (gram)	Diff(gram):
3		0	0			0	0			0	0	
4		60	0,74	0,74		60	1,65	1,65		60	0,93	0,93
5		120	1,08	0,34		120	2,38	0,73		120	1,68	0,75
6		180	1,58	0,50		180	3,05	0,67		180	2,36	0,68
7		240	2,08	0,50		240	3,68	0,63		240	2,97	0,61
8		300	2,54	0,46		300	4,28	0,60		300	3,52	0,55
9												
10	Trykk (bar):	2,84			Trykk (bar):	2,71			Trykk (bar):	2,71		
11												
12	Utveid (gram):	50,09			Utveid (gram):	50,04			Utveid (gram):	50,84		
13												
14	wt% fines (%):	5,07			wt% fines (%):	8,55			wt% fines (%):	6,92		
15												
16												
17												
18												
19	**Mg_Aluminat-Basis-1050C**				**Mg_Aluminat-Mølle-1050C**				**Alumina-Mølle**			
20		Tid (min):	Fines (gram)	Diff(gram):		Tid (min):	Fines (gram):	Diff(gram):		Tid (min):	Fines (gram)	Diff(gram):
21		0	0			0	0			0	0	
22		60	0,52	0,52		60	0,34	0,34		60	2,25	2,25
23		120	0,6	0,08		120	0,4	0,06		120	3,73	1,48
24		180	0,66	0,06		180	0,48	0,08		180	4,96	1,23
25		240	0,72	0,06		240	0,56	0,08		240	6,03	1,07
26		300	0,8	0,08		300	0,64	0,08		300	7,01	0,98
27												
28	Trykk (bar):	2,75			Trykk (bar):	2,71			Trykk (bar):	2,7		
29												
30	Utveid (gram):	50,11			Utveid (gram):	50,16			Utveid (gram):	50,2		
31												
32	wt% fines (%):	1,60			wt% fines (%):	1,28			wt% fines (%):	13,96		

Figure B.1: Attrition measurements

	A	B	C	D	E	F	G	H	I	J	K	L
1	**Mg_Aluminat-Basis-950C**				**Mg_Aluminat-Mølle-950C**				**Alumina-Basis**			
2		Tid (min):	Fines (gram):	Diff (gram):		Tid (min):	Fines (gram):	Diff(gram):		Tid (min):	Fines (gram):	Diff(gram):
3		0	0	0		0	0	0		0	0	0
4		60	0,5	0,50		60	0,67	0,67		60	0,68	0,68
5		120	1	0,50		120	1,3	0,63		120	1,29	0,61
6		180	1,46	0,46		180	1,9	0,60		180	1,84	0,55
7												
8												
9												
10												
11												
12	**Mg_Aluminat-Basis-1050C**				**Mg_Aluminat-Mølle-1050C**				**Alumina-Mølle**			
13		Tid (min):	Fines (gram):	Diff(gram):		Tid (min):	Fines (gram):	Diff(gram):		Tid (min):	Fines (gram):	Diff(gram):
14		0	0	0		0	0	0		0	0	0
15		60	0,06	0,06		60	0,08	0,08		60	1,23	1,23
16		120	0,12	0,06		120	0,16	0,08		120	2,3	1,07
17		180	0,2	0,08		180	0,24	0,08		180	3,28	0,98
18												

Figure B.2: Attrition measurements, linear part

B.2 Chemisorption data

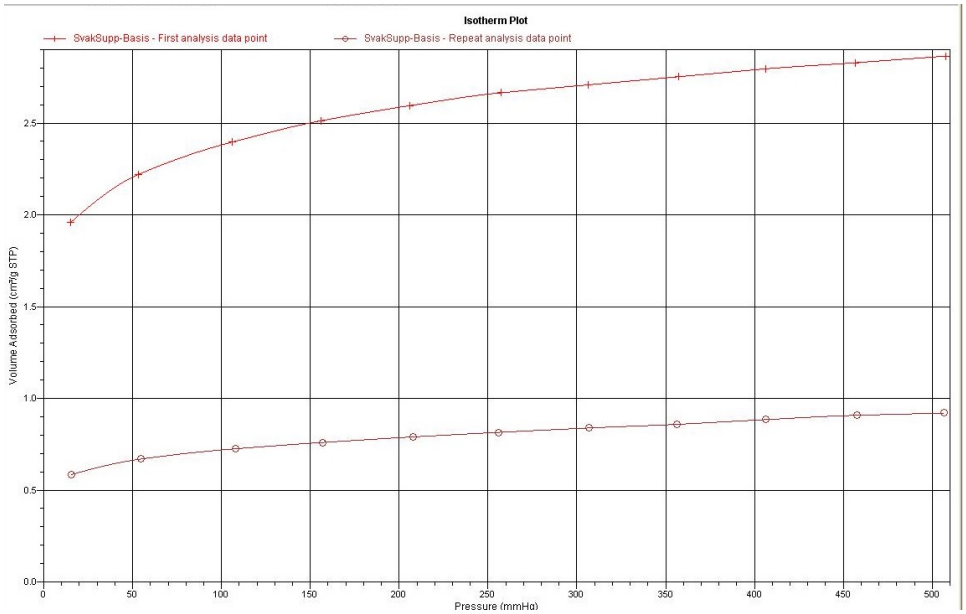

Figure B.3: Chemisorption isotherm plot weak support, basis

Analysis Summary

Element	Percent of Sample Weight (%)	Atomic Weight	Stoichiometry Factor	Atomic Cross-Sectional Area (nm^2)	Density (cm^3/g)
cobalt	12.000	58.933	2.000	0.0662	8.900

Analysis Results

Metal Dispersion:	10.4947 %
Metallic Surface Area:	8.5205 m^2/g sample
Metallic Surface Area:	71.0042 m^2/g metal
Crystallite Size (6.000 V / A):	9.49462 nm
Y-Intercept Quantity Adsorbed:	2.3949 ± 0.0223 cm^3/g STP
Slope:	0.000966 ± 0.000064
Correlation Coefficient:	9.87281E-01

Difference Results

Metal Dispersion:	7.4528 %
Metallic Surface Area:	6.0508 m^2/g sample
Metallic Surface Area:	50.4230 m^2/g metal
Crystallite Size (6.000 V / A):	13.37003 nm
Y-Intercept Quantity Adsorbed:	1.7007 ± 0.0185 cm^3/g STP
Slope:	0.000506 ± 0.000053
Correlation Coefficient:	9.69037E-01

Figure B.4: Chemisorption analysis results weak support, basis

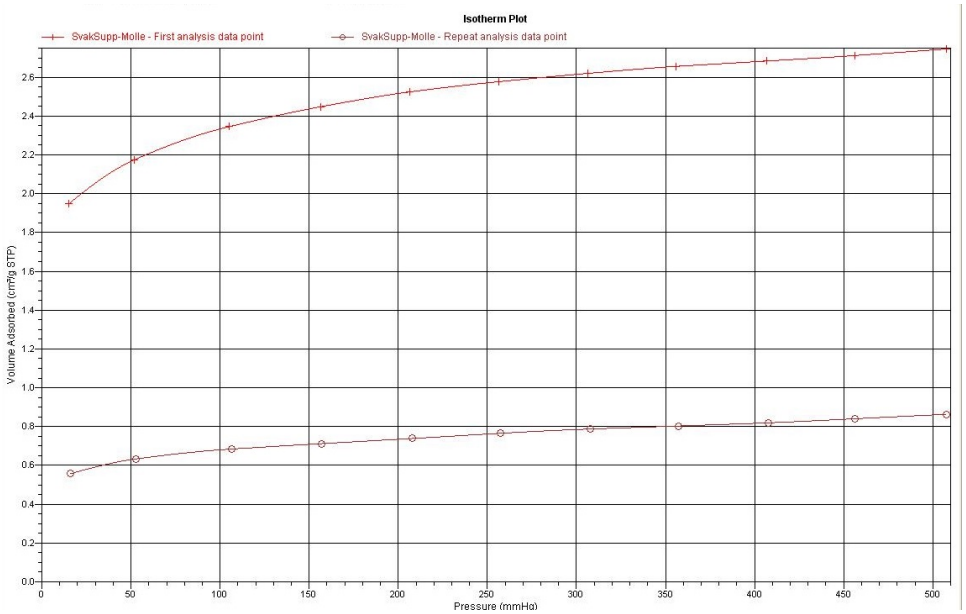

Figure B.5: Chemisorption isotherm plot weak support, milled

Analysis Summary

Element	Percent of Sample Weight (%)	Atomic Weight	Stoichiometry Factor	Atomic Cross-Sectional Area (nm^2)	Density (cm^3/g)
cobalt	12.000	58.933	2.000	0.0662	8.900

Analysis Results

Metal Dispersion:	10.3188 %
Metallic Surface Area:	8.3776 m^2/g sample
Metallic Surface Area:	69.8137 m^2/g metal
Crystallite Size (6.000 V / A):	9.65652 nm
Y-Intercept Quantity Adsorbed:	2.3547 ± 0.0211 cm^3/g STP
Slope:	0.000802 ± 0.000060
Correlation Coefficient:	9.83571E-01

Difference Results

Metal Dispersion:	7.4539 %
Metallic Surface Area:	6.0517 m^2/g sample
Metallic Surface Area:	50.4307 m^2/g metal
Crystallite Size (6.000 V / A):	13.36799 nm
Y-Intercept Quantity Adsorbed:	1.7010 ± 0.0170 cm^3/g STP
Slope:	0.000388 ± 0.000048
Correlation Coefficient:	9.56403E-01

Figure B.6: Chemisorption analysis results weak support, milled

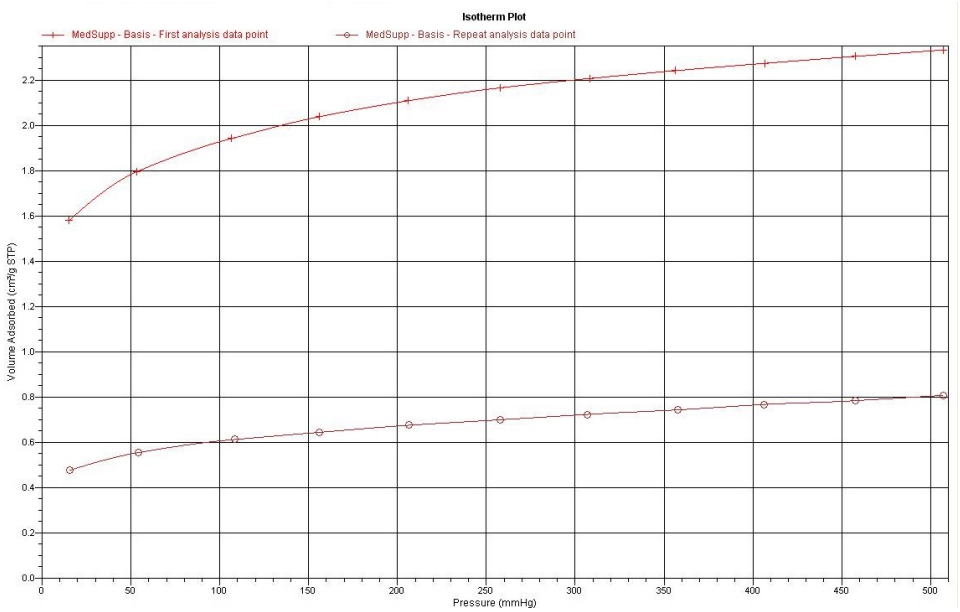

Figure B.7: Chemisorption isotherm plot medium support, basis

Analysis Summary

Element	Percent of Sample Weight (%)	Atomic Weight	Stoichiometry Factor	Atomic Cross-Sectional Area (nm^2)	Density (cm^3/g)
cobalt	12.000	58.933	2.000	0.0662	8.900

Analysis Results

Metal Dispersion:	8.5034 %
Metallic Surface Area:	6.9038 m^2/g sample
Metallic Surface Area:	57.5316 m^2/g metal
Crystallite Size (6.000 V / A):	11.71804 nm
Y-Intercept Quantity Adsorbed:	1.9405 ± 0.0195 cm^3/g STP
Slope:	0.000808 ± 0.000055
Correlation Coefficient:	9.86151E-01

Difference Results

Metal Dispersion:	5.9607 %
Metallic Surface Area:	4.8394 m^2/g sample
Metallic Surface Area:	40.3284 m^2/g metal
Crystallite Size (6.000 V / A):	16.71667 nm
Y-Intercept Quantity Adsorbed:	1.3602 ± 0.0154 cm^3/g STP
Slope:	0.000355 ± 0.000044
Correlation Coefficient:	9.57091E-01

Figure B.8: Chemisorption analysis results medium support, basis

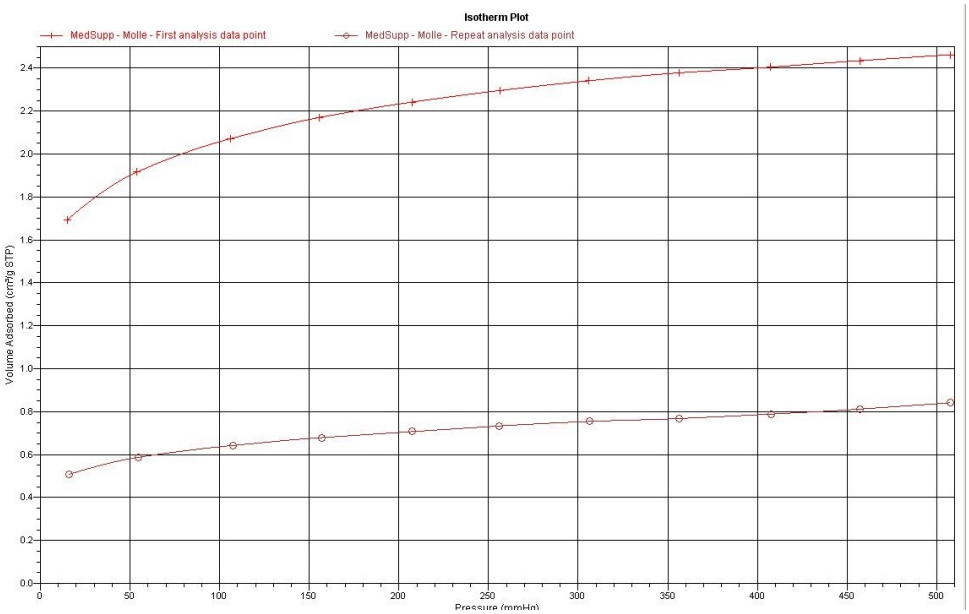

Figure B.9: Chemisorption isotherm plot medium support, milled

Analysis Summary

Element	Percent of Sample Weight (%)	Atomic Weight	Stoichiometry Factor	Atomic Cross-Sectional Area (nm^2)	Density (cm^3/g)
cobalt	12.000	58.933	2.000	0.0662	8.900

Analysis Results

Metal Dispersion:	9.0959 %
Metallic Surface Area:	7.3848 m^2/g sample
Metallic Surface Area:	61.5402 m^2/g metal
Crystallite Size (6.000 V / A):	10.95474 nm
Y-Intercept Quantity Adsorbed:	2.0757 ± 0.0211 cm^3/g STP
Slope:	0.000800 ± 0.000060
Correlation Coefficient:	9.83501E-01

Difference Results

Metal Dispersion:	6.3980 %
Metallic Surface Area:	5.1945 m^2/g sample
Metallic Surface Area:	43.2871 m^2/g metal
Crystallite Size (6.000 V / A):	15.57408 nm
Y-Intercept Quantity Adsorbed:	1.4600 ± 0.0199 cm^3/g STP
Slope:	0.000364 ± 0.000057
Correlation Coefficient:	9.34448E-01

Figure B.10: Chemisorption analysis results medium support, milled

B.3 Fischer-Tropsch synthesis data

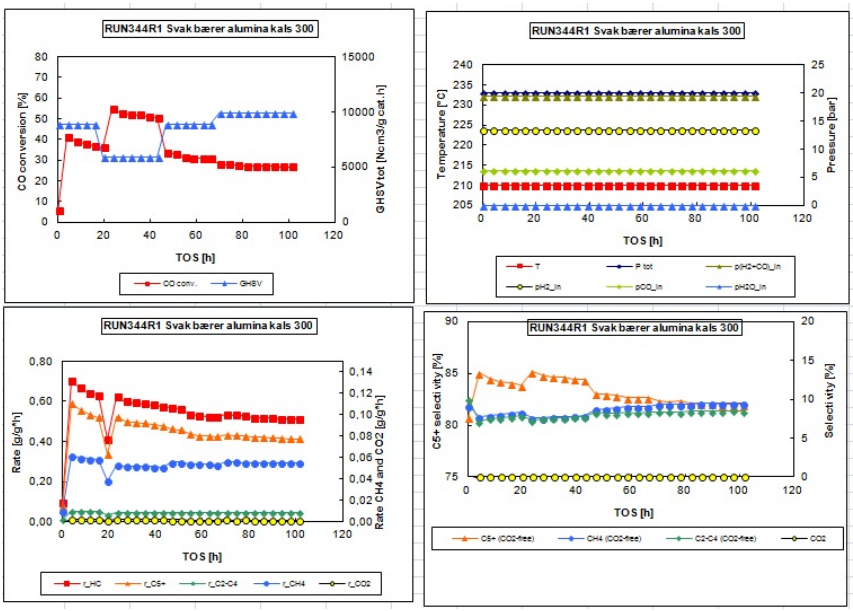

Figure B.11: FTS data 1, weak support

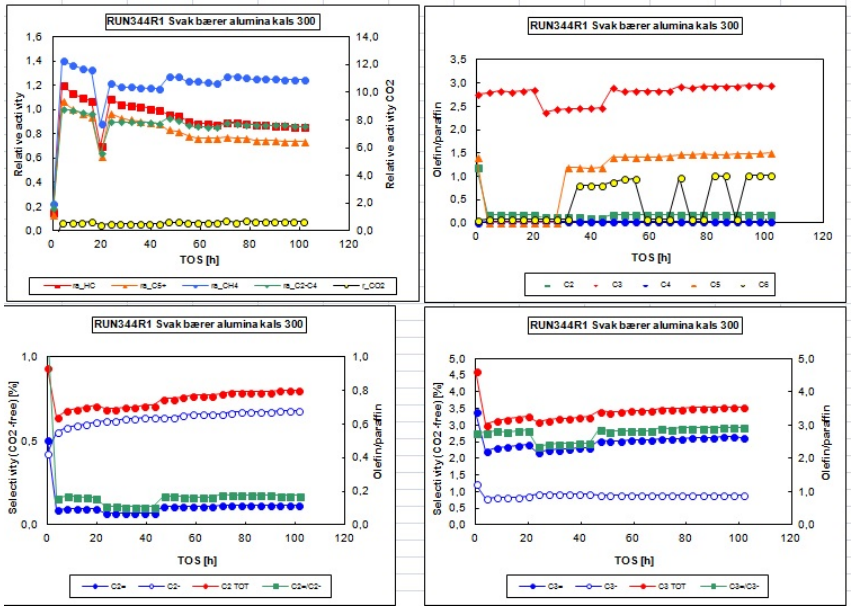

Figure B.12: FTS data 2, weak support

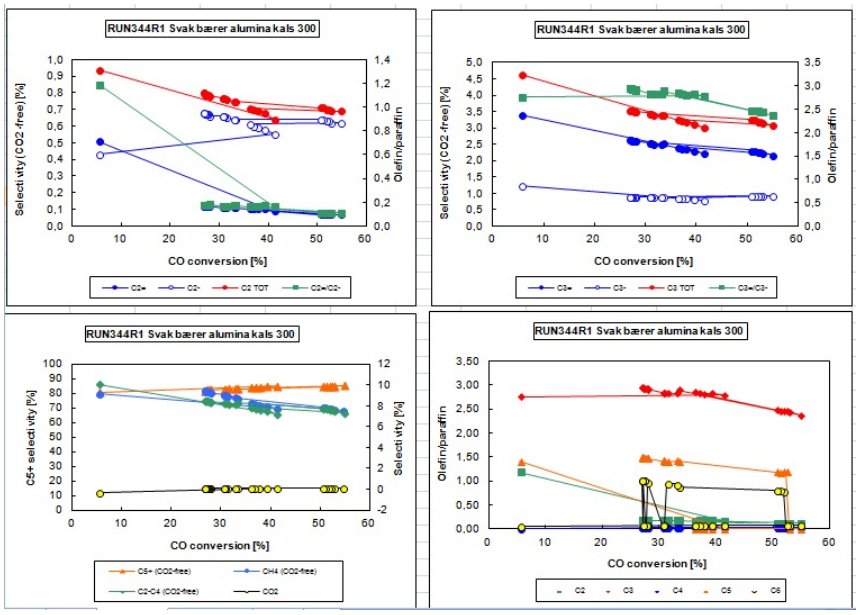

Figure B.13: FTS data 3, weak support

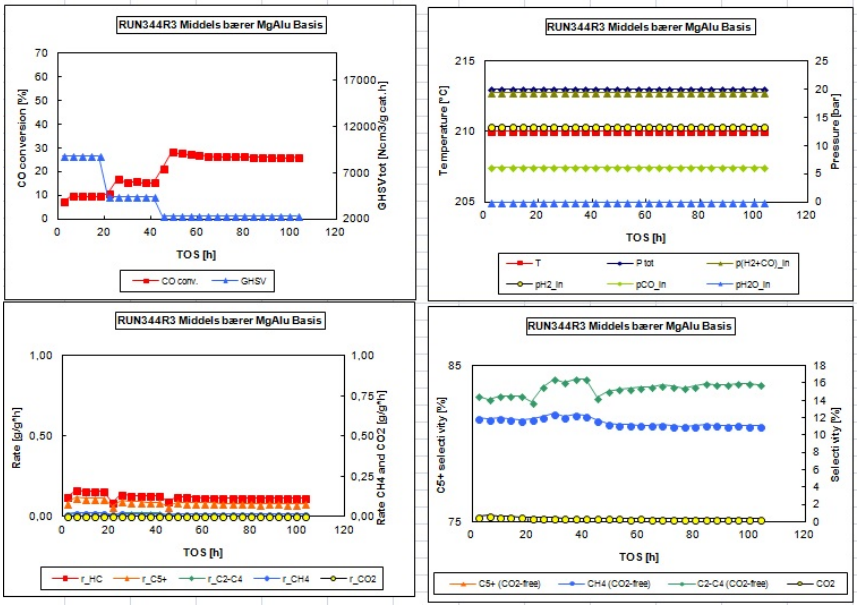

Figure B.14: FTS data 1, medium basis support

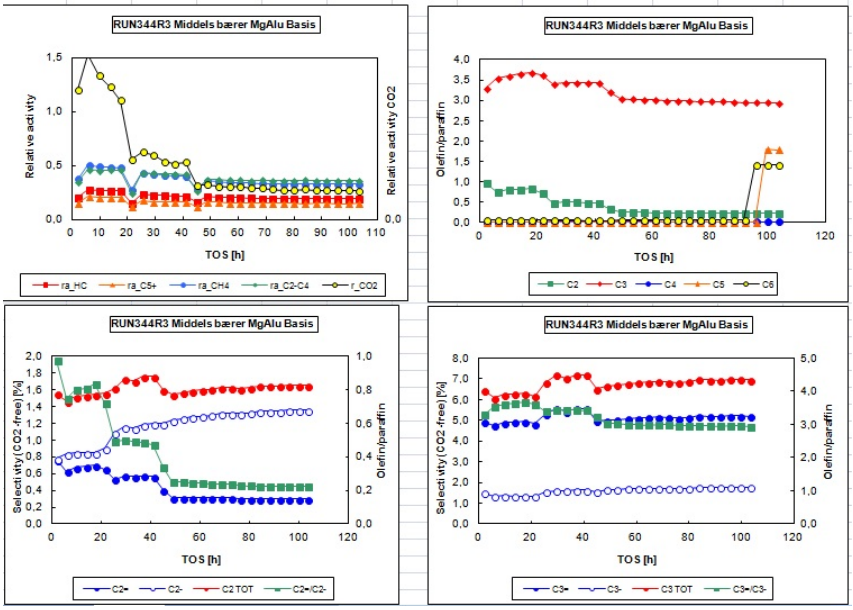

Figure B.15: FTS data 2, medium basis support

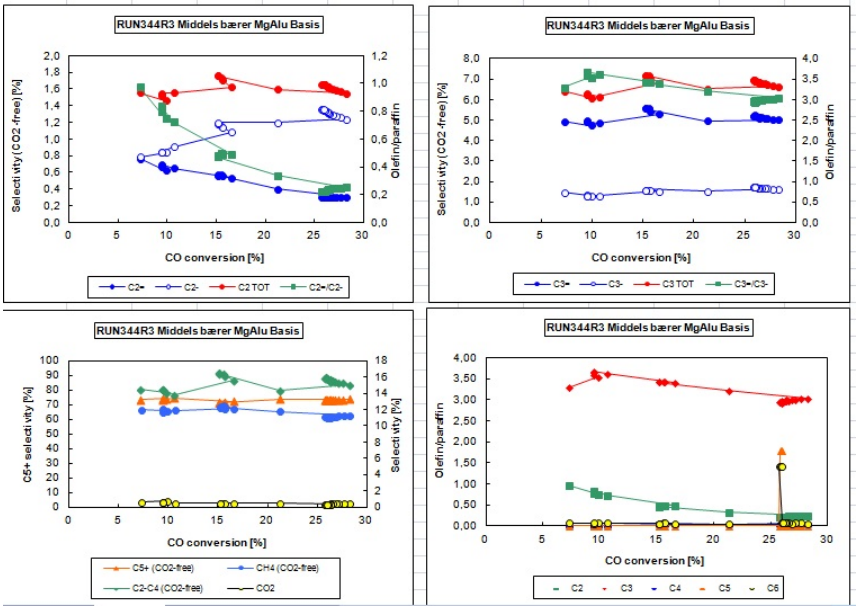

Figure B.16: FTS data 3, medium basis support

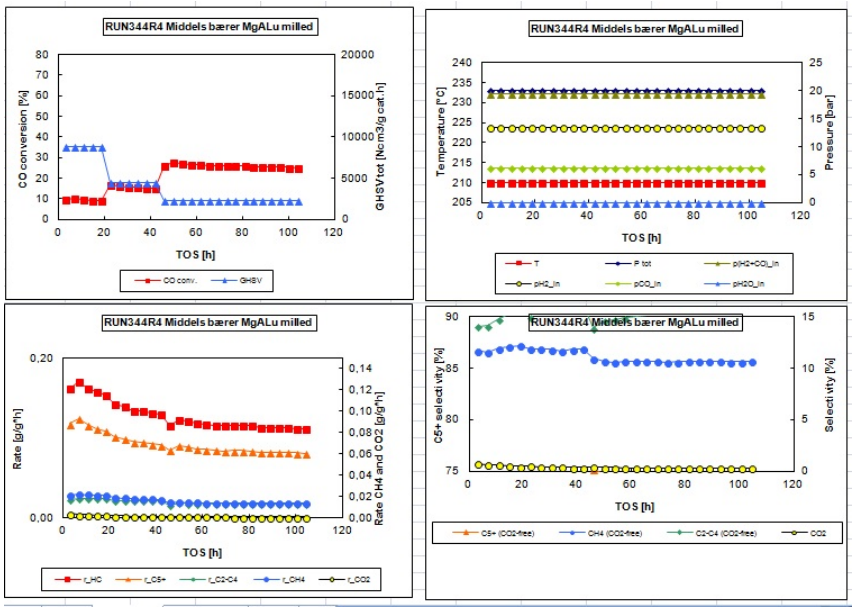

Figure B.17: FTS data 1, medium milled support

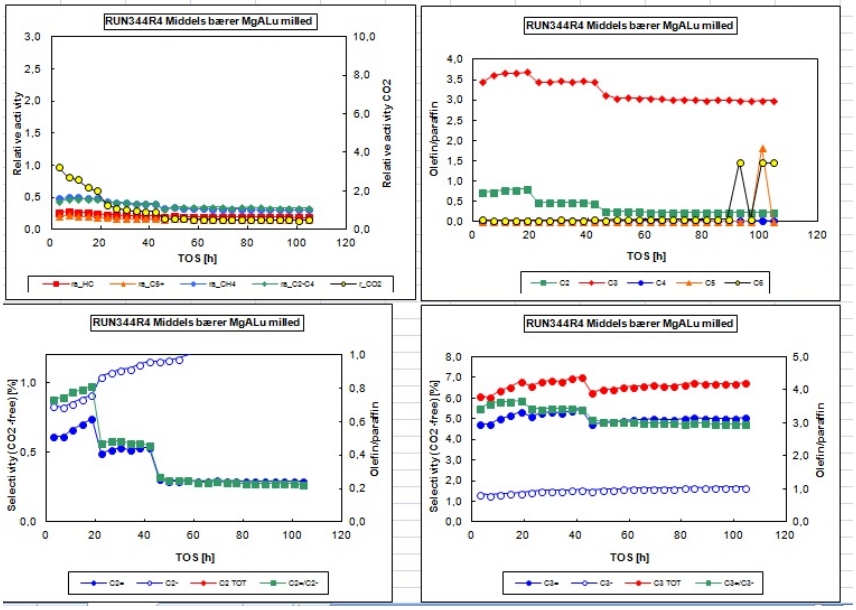

Figure B.18: FTS data 2, medium milled support

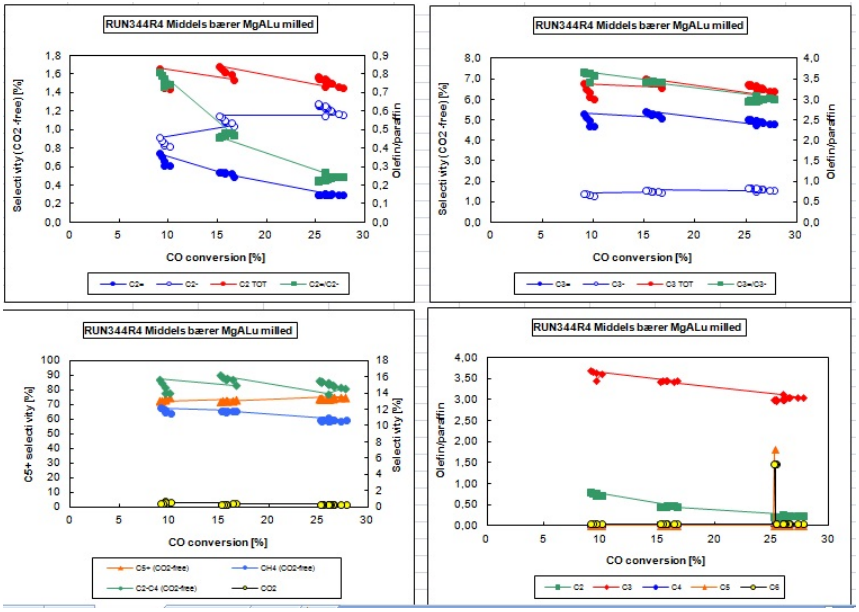

Figure B.19: FTS data 3, medium milled support

C Risk assessment

NTNU / HMS	Kartlegging av risikofylt aktivitet	Utarbeidet av: HMS-avd.	Nummer: HMSRV2601	Dato: 05.03.2010
		Godkjent av: Rektor	Side: 1 av 2	Erstatter: 01.12.2006

Enhet: IKP, NT-fakultetet, NTNU **Dato: 22.01.13**
Deltakere ved kartleggingen (m/ funksjon): Thomas Haukli Fiske, Torild Huslund Skagseth

Kort beskrivelse av hovedaktivitet/hovedprosess: Preparation and testing of catalyst support material

ID nr.	Aktivitet/prosess	Ansvarlig	Lov, forskrift o.l.	Eksisterende dokumentasjon	Eksisterende sikringstiltak	Kommentar
1.	Preparing catalyst		AML, kjemikalieforskriften	Datasheet, training	Safety gloves, safety glasses, ventilation	
2.	Filling nitrogen for BET		AML, kjemikalieforskriften	Datasheet, training	Cold resistant gloves, safety glasses,	
3.	Cleaning attrition rig		AML, kjemikalieforskriften	Datasheet, training, operating manual	Safety gloves, safety glasses, ventilation	

Figure C.1: Hazardous activity identification form

NTNU	Risikovurdering	utarbeidet av	Nummer	Dato	
		HMS-avd	HMSRV2603	4.3.2010	
HMS/KS		godkjent av	side	Erstatter	
		Rektor	1 av 3	9.2.2010	

Enhet: IKP, NT-fakultetet, NT **Dato: 22.01.13**
Linjeleder: Øyvind Gregersen
Deltakere ved risikovurderingen (m/ funksjon): Thomas Haukli Fiske, Torild Huslund Skagseth

ID nr	Aktivitet fra kartleggings-skjemaet	Mulig uønsket hendelse/ belastning	Vurdering av sannsyn-lighet	Vurdering av konsekvens:				Risiko-verdi	Kommentarer/status Forslag til tiltak
			(1-5)	Menneske (A-E)	Ytre miljø (A-E)	Øk/ materiell (A-E)	Om-dømme (A-E)		
1.	Preparing catalyst	Getting fine powders on skin, in eye, in mouth	2	A	A	A	A	A2	Working in ventilation cabinet with personal safety equipment minimizes risk for exposure
2.	Filling nitrogen for BET	Spilling liquid nitrogen on skin	2	B	A	A	A	B2	Lab coat and cold gloves minimizes risk for frost damage
3.	Cleaning attrition rig	Getting fine powders on skin, in eye, in mouth	3	A	A	A	A	A3	Wearing dust mask prevents dust from entering mouth and lungs

Figure C.2: Risk assessment

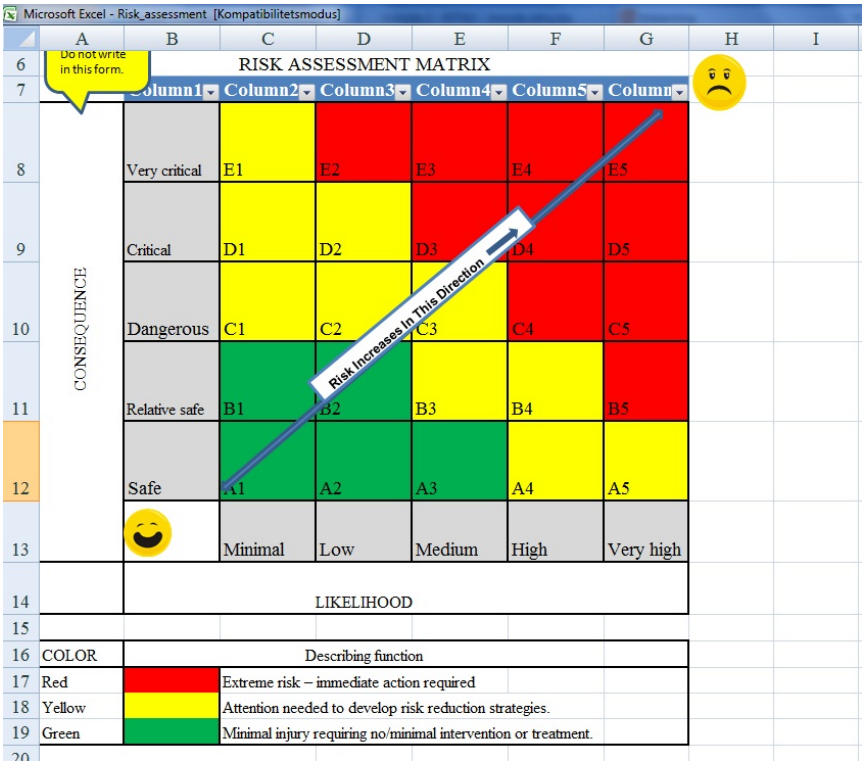

Figure C.3: Risk assessment matrix